

A local baseline of the black hole mass scaling relations for active galaxies. IV. Correlations between M_{BH} and host galaxy σ , stellar mass, and luminosity.

VARDHA N. BENNERT,¹ TOMMASO TREU,² XUHENG DING,^{3,2} ISAK STOMBERG,^{1,4,5,6} SIMON BIRRER,⁷ TOMAS SNYDER,¹ MATTHEW A. MALKAN,² ANDREW W. STEPHENS,⁸ AND MATTHEW W. AUGER⁹

¹*Physics Department, California Polytechnic State University, San Luis Obispo, CA 93407, USA*

²*Department of Physics, University of California, Los Angeles, CA 90095, USA*

³*Kavli Institute for the Physics and Mathematics of the Universe, The University of Tokyo, Kashiwa, Japan 277-8583 (Kavli IPMU, WPI)*

⁴*Department of Physics, KTH, Royal Institute of Technology, Stockholm, Sweden*

⁵*Universität Hamburg, Department of Physics, 20355 Hamburg, Germany*

⁶*Deutsches Elektronen-Synchrotron DESY, 22607 Hamburg, Germany*

⁷*Kavli Institute for Particle Astrophysics and Cosmology and Department of Physics, Stanford University, Stanford, CA 94305, USA*

⁸*Gemini Observatory/NSF's NOIRLab, 670 N. A'ohoku Place, Hilo, Hawai'i, 96720, USA*

⁹*Institute of Astronomy, Madingley Road, Cambridge CB3 0HA, UK*

ABSTRACT

The tight correlations between the mass of supermassive black holes (M_{BH}) and their host-galaxy properties have been of great interest to the astrophysical community, but a clear understanding of their origin and fundamental drivers still eludes us. The local relations for active galaxies are interesting in their own right and form the foundation for any evolutionary study over cosmic time. We present Hubble Space Telescope optical imaging of a sample of 66 local active galactic nuclei (AGNs); for 14 objects, we also obtained Gemini near-infrared images. We use state of the art methods to perform surface photometry of the AGN host galaxies, decomposing them in spheroid, disk and bar (when present) and inferring the luminosity and stellar mass of the components. We combine this information with spatially-resolved kinematics obtained at the Keck Telescopes to study the correlations between M_{BH} (determined from single-epoch virial estimators) and host galaxy properties. The correlations are uniformly tight for our AGN sample, with intrinsic scatter 0.2 – 0.4 dex, smaller than or equal to that of quiescent galaxies. We find no difference between pseudo and classical bulges or barred and non-barred galaxies. We show that all the tight correlations can be simultaneously satisfied by AGN hosts in the 10^7 - $10^9 M_{\odot}$ regime, with data of sufficient quality. The $M_{\text{BH}}-\sigma$ relation is also in agreement with that of AGNs with M_{BH} obtained from reverberation mapping, providing an indirect validation of single-epoch virial estimators of M_{BH} .

Keywords: accretion, accretion disks – black hole physics – galaxies: active – galaxies: evolution – galaxies: Seyfert

1. INTRODUCTION

When growing through accretion, supermassive black holes (BHs) can be seen as bright nuclei in active galaxies (AGNs). The observed relations between the mass of the BH (M_{BH}) and the properties of the host-galaxy spheroid such as luminosity, stellar mass and stellar-velocity dispersion σ , are thought to result from the co-

evolution between BHs and galaxies (for a review see, e.g., Kormendy & Ho 2013; Graham 2016). Such a co-evolution is either regulated by AGN feedback (e.g., Di Matteo et al. 2005; Croton 2006; Dubois et al. 2013, 2016; DeGraf et al. 2015; Hopkins et al. 2016), or hierarchical assembly of M_{BH} and stellar mass through galaxy merging (e.g., Peng 2007; Hirschmann et al. 2010; Jahnke & Maccio 2011). To shed light on the origin of these relations, recent years have seen an explosion of observational studies both in the local Universe (e.g., Ferrarese & Ford 2005; Greene & Ho 2006; Gültekin et al. 2009; Bennert et al. 2011a; Kormendy et al. 2011;

Beifiori et al. 2012; Läscher et al. 2016; Davis et al. 2018; Sahu et al. 2019) and as a function of cosmic history (e.g. Treu et al. 2004; Peng et al. 2006a,b; Woo et al. 2006; Salvander et al. 2007; Riechers et al. 2009; Jahnke et al. 2009; Bennert et al. 2010; Decarli et al. 2010; Merloni et al. 2010; Bennert et al. 2011b; Park et al. 2015; Sexton et al. 2019; Silverman et al. 2019; Ding et al. 2020).

By necessity, all studies beyond the local Universe focus on broad-line (or type-1) AGNs (BLAGNs). For BLAGNs, M_{BH} can be estimated to within a factor of 2-3 using empirically calibrated relations based on a sample of reverberation-mapped AGNs. Reverberation mapping (RM) is a technique that studies the time delay between the variability of the accretion disk and the response of ionized gas in the vicinity of the BH, the broad-line region (BLR) (e.g., Wandel et al. 1999; Woo & Urry 2002; Vestergaard 2002; Vestergaard & Peterson 2006; McGill et al. 2008). Using light-travel time arguments, the time delay translates into a size of the BLR. Combining the size with the Doppler-broadened width of the emission lines (e.g., the Hydrogen Balmer series in the optical) results in an estimate of the M_{BH} up to an unknown factor that depends on the geometry and kinematics of the gas clouds. Traditionally, this factor f (also known as virial factor) has been derived as a sample average by matching the scaling relation between M_{BH} and (spheroid) stellar-velocity dispersion σ of the RM AGNs with that of quiescent galaxies (e.g., Onken et al. 2004; Park et al. 2012; Woo et al. 2010, 2015). More recently, dynamical modeling of RM data has been used to constrain both geometry and kinematics of the BLR and thus determine M_{BH} for individual objects, finding consistent results (e.g., Brewer et al. 2011; Pancoast et al. 2011; Li et al. 2013; Pancoast et al. 2018; Williams et al. 2018, 2020). While RM is time-consuming, the RM AGN sample revealed a relation between BLR size and AGN luminosity that can be used to estimate M_{BH} for BLAGNs from one spectrum, known as the single-epoch method. In the single-epoch virial estimation, the width of broad emission lines is combined with the AGN luminosity which serves as a proxy for BLR size. As such, the RM AGN sample serves as a M_{BH} calibrator beyond the local Universe. The single-epoch method has been used for virial mass estimates of hundreds of thousands of AGNs (e.g., Rakshit et al. 2020), across cosmic history (e.g., Mortlock et al. 2011), to study the cosmic evolution of the M_{BH} scaling relations (e.g., Treu et al. 2004; Peng et al. 2006a; Woo et al. 2006; Bennert et al. 2010; Merloni et al. 2010; Park et al. 2015; Ding et al. 2020) and distribution of Eddington ratios (e.g., Shen 2013).

Studies of the evolution of the M_{BH} -host-galaxy scaling relations with redshift constrain theoretical interpretations and shed light onto their origin (e.g., Croton 2006; Hopkins et al. 2007); however, they depend on our understanding of the slope and intrinsic scatter of local relations, in particular those for active galaxies. Moreover, studying dependencies of the correlations on bulge structure and other morphological components at high-redshifts is difficult if not impossible, especially given the presence of the bright AGN point source in the center. Late-type galaxies are often known to host pseudo-bulges, characterized by exponential light profiles, ongoing star formation or starbursts, and nuclear bars. It is generally believed that they have evolved secularly through dissipative processes rather than mergers (e.g., Courteau et al. 1996; Kormendy & Kennicutt 2004). Classical bulges, in contrast, are thought of as centrally concentrated, mostly red and quiescent, merger-induced systems. Pseudo-bulges and minor mergers provide a valuable test of some hypotheses for the origin of the M_{BH} scaling relations: if they lie on the relation, as found by our results based on SDSS images (Bennert et al. 2015), it could indicate that secular evolution has a synchronizing effect, growing BHs and bulges simultaneously at a small but steady rate for late-type galaxies (Cisternas et al. 2011a,b).

This paper is the last of a series aimed at creating a robust local baseline of the M_{BH} scaling relations of BLAGNs for comparison with high redshift studies. We selected a sample of ~ 100 Seyfert-1 galaxies from SDSS ($0.02 \leq z \leq 0.1$; $M_{\text{BH}} > 10^7 M_{\odot}$) based on their broad $\text{H}\beta$ emission in the same fashion as high-redshift samples used for evolutionary studies (Bennert et al. 2010; Park et al. 2015; Ding et al. 2020), allowing for a direct comparison. The majority of AGNs ($\sim 80\%$) in our sample reside in galaxies classified as Sa or later (Bennert et al. 2015), comparable to our high-redshift samples (Bennert et al. 2010; Park et al. 2015), perhaps not surprisingly, given that all studies focus on Seyfert-1 galaxies. In paper I and III (Bennert et al. 2011a, 2015), multi-filter SDSS images yielded photometric parameters such as the spheroid effective radius, the spheroid luminosity, the host-galaxy free 5100Å luminosity of the AGN (for an accurate M_{BH} measurement), and spheroid stellar masses. In paper II (Harris et al. 2012), high-quality long-slit Keck/LRIS spectra provided both M_{BH} estimates as well as accurate spatially-resolved stellar-velocity dispersions (σ) and rotation curves.

Given the wide range of M_{BH} , host-galaxy morphologies, and stellar masses, our sample is well suited to determine the slope and intrinsic scatter of the local

scaling relations and to study dependencies on other parameters such as bulge structure and mergers. However, relying on low-quality optical photometry (such as SDSS) whose insufficient angular resolution and limited sensitivity to dust extinction significantly increase observational scatter in the M_{BH} scaling relations, ultimately limits conclusive results. High-resolution images are essential to resolve (pseudo-) bulges, given that roughly half of all objects have bulge effective radii smaller than $\sim 1.5''$ (corresponding to ~ 1.7 kpc for a typical distance of the galaxies in our sample; Bennert et al. 2015). This is not only crucial for proper morphological classification and determination of bulge luminosity, it also is important for the effective radius measurement. The latter, in turn, is important for a robust measurement of spatially-resolved stellar-velocity dispersion within the effective spheroid radius (Bennert et al. 2015). In other words, angular resolution is the key for an accurate determination of all M_{BH} scaling relations.

In this paper, to overcome these problems and to obtain high-quality host-galaxy images, we took a two-pronged approach. A sub-set of the parent sample (15 objects), selected to cover a wide range of morphologies (as based on SDSS images), was observed with the Near InfraRed Imager and spectrograph (NIRI) on Gemini North. Gemini-NIRI was chosen (i) for its high-spatial resolution (instrument plus site seeing) to distinguish between classical and pseudo-bulges in the presence of an AGN point source; (ii) for its large field-of-view ($2' \times 2'$ at f/6) to measure the surface brightness profile of these nearby galaxies out to large radii; and (iii) because near-infrared observations maximize the contrast between AGN and host and minimize dust extinction, revealing the presence of (pseudo-) bulges, bars and (minor) mergers. The reduced dust extinction also makes NIR luminosities a better tracer of stellar mass. At the same time, the parent sample was part of a Hubble Space Telescope (HST) snapshot (SNAP) program (PI Bennert). HST images provide both a high spatial resolution and a stable point-spread function (PSF). WFC3/UVIS was used with broad-band filter F814W to maximize the contrast between AGN and host, avoiding strong AGN emission lines, while taking full advantage of the high resolution of UVIS. Compared to existing SDSS images, the HST images have a factor of ~ 40 increase in resolution. A total of 66 objects were observed with HST, 14 of which also have Gemini images. Gemini and HST images naturally complement each other and to-

gether provide a long wavelength range for stellar-mass determination for overlapping objects. By construction, SDSS images in five filters are available for all objects to further assist in constraining stellar masses. Combining the high-quality spectroscopic data (paper II) with high-quality imaging provides a representative spectral and spatial coverage of supermassive BHs and their hosts for a detailed mapping of the local M_{BH} scaling relations for active galaxies and their underlying drivers.

The paper is organized as follows. Section 2 summarizes the sample selection, HST and Gemini observations, and data reduction. Section 3 describes the analysis and derived quantities. Section 4 presents host-galaxy morphologies and discusses the resulting M_{BH} scaling relations. Section 5 concludes with a summary. Throughout this paper, magnitudes are given in AB magnitudes. For conversion to luminosities, absolute solar magnitudes were taken from Willmer (2018) and a Hubble constant of $H_0 = 70 \text{ km s}^{-1}$ and a flat Universe with a cosmological constant of $\Omega_\lambda = 0.7$ are assumed.

2. SAMPLE SELECTION, OBSERVATIONS, AND DATA REDUCTION

2.1. Sample selection

The parent sample is 102 type-1 Seyfert galaxies selected from the Sloan Digital Sky Survey (SDSS) data release six (Adelman-McCarthy et al. 2008) based on redshift ($0.02 \leq z \leq 0.1$) and $M_{\text{BH}} (> 10^7 M_\odot)$, and observed with Keck/LRIS, presented in detail in papers I, II and III in this series (Bennert et al. 2011a; Harris et al. 2012; Bennert et al. 2015). Accurate spatially-resolved stellar-velocity dispersions were obtained for 84 objects (paper II) and formed the sample for our HST snapshot (SNAP) program. 15 objects with a wide variety of host-galaxy properties, as determined from SDSS images (Bennert et al. 2015), were observed with NIRI on Gemini North (PI: Bennert; program ID GN-2016B-Q-33). 68 objects were observed as part of HST SNAP, although we were unable to determine a robust M_{BH} for 2 of them due to a lack of broad $H\beta$ in the Keck spectrum (despite it being present in prior SDSS spectra; Runco et al. 2016). Of the remaining 66, 14 overlap with the Gemini sample. Fully-reduced SDSS images are available for all objects through the SDSS archive. Sample properties (coordinates, redshift and host-galaxy morphology) can be found in Table 1.

Table 1. Sample and host-galaxy properties

Object	R.A.	Decl.	z	Frame	Host	n	B2T	rot.	bar
(1)	(J2000) (2)	(J2000) (3)	(4)	(") (5)	(6)	(7)	(8)	(9)	(10)
0013-0951	00 13 35.38	-09 51 20.9	0.0615	21.7	BD (C)	Y	Y	N	N
0038+0034	00 38 47.96	+00 34 57.5	0.0805	18.9	BD (C)	N	N	N	N
0109+0059	01 09 39.01	+00 59 50.4	0.0928	14.0	BDB (P)	Y	Y	N	Y
0121-0102	01 21 59.81	-01 02 24.4	0.054	28.0	BDB (P)	Y	Y	N	Y
0150+0057	01 50 16.43	+00 57 01.9	0.0847	21.7	BDB (P)	Y	Y	N	Y
0206-0017	02 06 15.98	-00 17 29.1	0.043	56.0	BD (C)	N	N	N	N
0212+1406	02 12 57.59	+14 06 10.0	0.0618	21.7	BDB (P)	Y	Y	N	Y
0301+0110	03 01 24.20	+01 10 22.1	0.0715	14.0	BD (C)	N	N	N	Y
0301+0115	03 01 44.19	+01 15 30.8	0.0747	12.6	BDB (P)	Y	Y	N	Y
0336-0706	03 36 02.09	-07 06 17.1	0.097	23.8	BD (P)	Y	Y	N	Y
0353-0623	03 53 01.02	-06 23 26.3	0.076	19.6	BDB (C)	Y	Y	N	N
0737+4244	07 37 03.28	+42 44 14.6	0.0882	14.0	BD (C)	N	Y	N	N
0802+3104	08 02 43.40	+31 04 03.3	0.0409	19.6	BDB (P)	Y	Y	N	Y
0811+1739	08 11 10.28	+17 39 43.9	0.0649	21.7	BDB (P)	Y	Y	N	Y
0813+4608	08 13 19.34	+46 08 49.5	0.054	23.8	BDB (C)	N	Y	N	Y
0845+3409	08 45 56.67	+34 09 36.3	0.0655	28.0	BDB (C)	N	Y	N	Y
0857+0528	08 57 37.77	+05 28 21.3	0.0586	19.6	BD (C)	Y	Y	N	N
0904+5536	09 04 36.95	+55 36 02.5	0.0371	31.5	BD (C)	Y	N	N	N
0909+1330	09 09 02.37	+13 30 18.2	0.0506	31.5	BDB (P)	Y	Y	N	Y
0921+1017	09 21 15.55	+10 17 40.9	0.0392	39.2	BD (C)	N	Y	N	N
0923+2254	09 23 43.00	+22 54 32.7	0.0332	47.6	BDB (P)	Y	Y	N	Y
0923+2946	09 23 19.73	+29 46 09.1	0.0625	19.6	B (C)	N	N	N	N
0927+2301	09 27 18.51	+23 01 12.3	0.0262	59.5	BD (C)	Y	Y	N	N
0932+0233	09 32 40.55	+02 33 32.6	0.0567	17.5	BD (C)	Y	Y	N	N
0936+1014	09 36 41.08	+10 14 15.7	0.06	39.2	BD (C)	Y	Y	N	N
1029+1408	10 29 25.73	+14 08 23.2	0.0608	28.0	BD (C)	N	N	N	N
1029+2728	10 29 01.63	+27 28 51.2	0.0377	19.6	BD (C)	N	N	N	N
1029+4019	10 29 46.80	+40 19 13.8	0.0672	15.4	BD (C)	Y	Y	N	N
1042+0414	10 42 52.94	+04 14 41.1	0.0524	17.5	BDB (P)	Y	Y	N	Y
1043+1105	10 43 26.47	+11 05 24.3	0.0475	14.0	B (C)	N	N	N	N
1058+5259	10 58 28.76	+52 59 29.0	0.0676	23.8	BDB (P)	Y	Y	N	Y
1101+1102	11 01 01.78	+11 02 48.8	0.0355	28.0	BD (C)	N	N	Y	N
1104+4334	11 04 56.03	+43 34 09.1	0.0493	12.6	BDB (C)	N	N	N	Y
1137+4826	11 37 04.17	+48 26 59.2	0.0541	7.7	BD (C)	N	N	N	N
1143+5941	11 43 44.30	+59 41 12.4	0.0629	31.5	BDB (C)	N	Y	N	Y
1144+3653	11 44 29.88	+36 53 08.5	0.038	31.5	BD (C)	Y	Y	N	N
1145+5547	11 45 45.18	+55 47 59.6	0.0534	28.0	BDB (C)	Y	Y	N	N
1147+0902	11 47 55.08	+09 02 28.8	0.0688	19.6	BD (C)	N	N	N	N
1205+4959	12 05 56.01	+49 59 56.4	0.063	28.0	BD (C)	N	Y	N	N
1206+4244	12 06 26.20	+42 44 26.95	0.052	28.0	BDB (P)	Y	Y	N	Y
1216+5049	12 16 07.09	+50 49 30.0	0.0308	47.6	BD (C)	N	Y	N	N
1223+0240	12 23 24.14	+02 40 44.4	0.0235	28.0	BD (C)	N	Y	N	N
1246+5134	12 46 38.74	+51 34 55.9	0.0668	17.5	BD (P)	Y	Y	Y	N
1306+4552	13 06 19.83	+45 52 24.2	0.0507	23.8	BDB (P)	Y	Y	N	Y

Table 1 *continued*

Table 1 (*continued*)

Object	R.A.	Decl.	z	Frame	Host	n	B2T	rot.	bar
	(J2000)	(J2000)		(")					
(1)	(2)	(3)	(4)	(5)	(6)	(7)	(8)	(9)	(10)
1307+0952	13 07 21.93	+09 52 09.3	0.049	23.8	BDB (P)	Y	Y	N	Y
1312+2628	13 12 59.59	+26 28 24.0	0.0604	28.0	BDB (P)	Y	Y	N	Y
1405-0259	14 05 14.86	-02 59 01.2	0.0541	23.8	BD (C)	Y	Y	N	N
1416+0137	14 16 30.82	+01 37 07.9	0.0538	39.2	BD (C)	N	Y	N	N
1419+0754	14 19 08.30	+07 54 49.6	0.0558	35.7	BD (P)	Y	Y	Y	N
1434+4839	14 34 52.45	+48 39 42.8	0.0365	31.5	BDB (P)	Y	Y	N	Y
1545+1709	15 45 07.53	+17 09 51.1	0.0481	15.4	BD (C)	N	N	N	N
1557+0830	15 57 33.13	+08 30 42.9	0.0465	7.7	B (C)	N	N	N	N
1605+3305	16 05 02.46	+33 05 44.8	0.0532	15.4	BD (C)	Y	Y	N	N
1606+3324	16 06 55.94	+33 24 00.3	0.0585	26.6	BD (C)	N	N	N	N
1611+5211	16 11 56.30	+52 11 16.8	0.0409	19.6	BD (C)	N	N	N	N
1636+4202	16 36 31.28	+42 02 42.5	0.061	29.4	BDB (C)	N	N	N	Y
1708+2153	17 08 59.15	+21 53 08.1	0.0722	28.0	BD (P)	Y	Y	Y	N
2116+1102	21 16 46.33	+11 02 37.3	0.0805	23.8	BDB (P)	Y	Y	N	Y
2140+0025	21 40 54.55	+00 25 38.2	0.0838	14.0	BD (C)	Y	Y	N	N
2215-0036	22 15 42.29	-00 36 09.6	0.0992	19.6	BD (C)	Y	Y	N	N
2221-0906	22 21 10.83	-09 06 22.0	0.0912	12.6	BD (C)	N	Y	N	N
2222-0819	22 22 46.61	-08 19 43.9	0.0821	19.6	BDB (P)	Y	Y	N	Y
2233+1312	22 33 38.42	+13 12 43.5	0.0934	31.5	BDB (P)	Y	Y	N	Y
2254+0046	22 54 52.24	+00 46 31.4	0.0907	31.5	BD (C)	Y	N	N	N
2327+1524	23 27 21.97	+15 24 37.4	0.0458	31.5	BD (C)	N	N	N	N
2351+1552	23 51 28.75	+15 52 59.1	0.0963	19.6	BD (C)	N	Y	N	N

NOTE— Col. (1): Target ID used throughout the text (based on R.A. and declination). Col. (2): Right ascension in hours, minutes and seconds. Col. (3): Declination in degrees, arcminutes and arcseconds. Col. (4): Redshift from SDSS data release seven (Abazajian et al. 2009). Col. (5): Frame size of image shown in Figs. 1-3 (in arcsecond, in x and y). Col. (6): Host-galaxy fit (B: spheroid only, BD: spheroid+disk, BDB: spheroid+disk+bar). In parentheses: Spheroid component: C = classical bulge; P = pseudo-bulge. Col. (7-10): Criteria for classification of bulge as pseudo-bulge. If at least three of these four criteria are met, the bulge is classified as pseudo-bulge. Col. (7): Sérsic index $n < 2$. Col. (8): Bulge-to-total luminosity ratio < 0.5 . Col. (9): Rotation dominated (i.e., ratio between maximum rotational velocity at effective spheroid radius and central stellar-velocity dispersion > 1). Col. (10): Presence of a bar for face-on galaxies.

2.2. HST observations and data reduction

84 objects were part of an HST SNAP program (HST GO 15215 and HST GO 16014, PI Bennert; Cycles 25-27), yielding images for 68 AGN host galaxies, a completion rate of almost 80% (significantly higher than the 30% typical for SNAP programs). To obtain the dynamic range needed for an accurate decomposition of the host galaxy and the AGN, the long exposures (400 seconds) were complemented by short, unsaturated ones (between 20-100 seconds, depending on the object's brightness). To avoid buffer dump (which occurred during the long exposures), a sequence of one short and one long exposure at the same location was followed by another sequence of one long and one short exposure at a dithered location. POS TARG was used to set up

a dither pattern manually that corresponds to the default WFC3-UVIS-GAP-LINE (with center UVIS). Full-frame images were read to trace the host-galaxy disks out to the background and to obtain field stars for PSF fitting of the strong AGN point source in the center.

Data processed through the standard WFC3 calibration pipeline were retrieved from the HST archive. L.A. Cosmic (Laplacian Cosmic Ray Identification) (van Dokkum 2001) was run to remove cosmic rays. All long exposures were carefully checked for saturation, especially of the bright AGN point source. For objects with saturated pixels, the short exposures taken at the same dither location as the long ones were scaled according to exposure time and used to replace the saturated pixels. Pyraf package astrodrizzle was then used to combine the two long exposures. A wide

range of combinations of the final drizzle parameters scale and pixfrac were applied. After careful examination of the images and based on resolution, image quality and FWHM of the PSF, the following parameters were adopted: `driz_sep_bits=336`, `final_bits=336`, `final_wcs=yes`, `final_pixfrac=0.9`, `final_scale=0.035`, resulting in a final pixel scale of $0.035''/\text{pix}$. For objects without any saturated pixels, the long exposures were combined with `astrodrizzle` directly in the same way. Final images are shown in Figures 1-3.

2.3. Gemini observations and data reduction

15 Seyfert-1 galaxies were selected from the parent sample covering a wide range of morphologies (based on SDSS images). All galaxies were observed with NIRI on Gemini North with the largest field-of-view (FOV; $2' \times 2'$ at $f/6$; pixel scale of $0.117''$) in Ks band. Observations have an average FWHM of $0.33''$ ($0.24 - 0.44''$) and were obtained at airmass less than 1.5. This image quality is 3-4 times better than the SDSS images which have a typical seeing of $1.5''$. Exposure times range between 2-10 seconds per image with 3-6 co-adds and 18-24 images on source, resulting in a total exposure time of 144-540 seconds, depending on the brightness of the object. The sky positions were observed with guiding enabled and were carefully selected to include a nearby bright field star. This ensured that we could generate accurate PSF models for every galaxy. Details of the observations are given in Table 2.

Data reduction was performed following standard procedures using the Gemini IRAF (Tody 1986, 1993) package customized for NIRI and included dark subtraction and flat fielding using off-target exposures. Flux calibration was obtained by standard IRAF photometry of UKIRT faint standard stars observed directly before or after the science images. Absolute magnitudes take into account extinction (Schlafly & Finkbeiner 2011); Ks-band luminosities were determined assuming an absolute Ks-band magnitude of the Sun of $M_{Ks} = 5.08$ (Willmer 2018) Resulting images are shown in Figure 4.

3. DERIVED QUANTITIES

3.1. Surface photometry

To perform a detailed 2D host-galaxy fitting, we use the public image analysis software `lenstronomy`¹ (Birrer et al. 2018). `Lenstronomy` supersedes `GALFIT` (Peng et al. 2002) by applying an MCMC technique to provide realistic errors and explore the covariance between the various model parameters. It allows for a more general

surface brightness reconstruction possible with a large non-parametric basis set; the coefficients are determined through a linear minimization rather than a non-linear parameter fitting (Birrer et al. 2015). Also, iterative PSF reconstruction is possible and allows one to incorporate residual uncertainties due to PSF mismatch into the analysis. While `lenstronomy` was originally developed for galaxy-scale strong gravitational lensing, it has a much broader application, including general 2D galaxy decompositions.

A well subtracted background and a matching PSF is important for obtaining reliable host galaxy properties from 2D surface photometry. We estimate and remove the local background light in 2D space based on the `SExtractorBackground` algorithm built in the `photutils` package (Python based), which effectively accounts for gradients in the background light distribution. For all objects, PSF stars were created from suitable stars in the field-of-view (FOV) of each object, following the criteria: bright, unsaturated star without any nearby objects, located close to the AGN/center of the FOV and an overall profile as expected for a PSF star. These individual PSF stars were then recentered and stacked, resulting in a PSF with high signal-to-noise ratio (S/N), centered in the image. Each individual PSF star was recentered using `AstroObjectAnalyzer`² through an iterative interpolation algorithm. Finally, masks were created to mask any nearby sources. Three objects have close-by neighboring galaxies which were fitted simultaneously.

The central AGN was fitted by a PSF, the host galaxies with three different models: (1) a spheroid-only component (free Sérsic index n ; Sérsic 1963); (2) a spheroid plus disk component (Sérsic index = 1) (3) a spheroid plus disk plus bar component (Sérsic index = 0.5). Based on pre-defined starting parameters and constraints, `lenstronomy` determines the maximum likelihood fit adopting a Particle Swarm Optimizer (PSO) (Kennedy & Eberhart 2001). We use the following limits: effective radius r_{eff} for all components: $3 \times \text{pixel size} \leq r_{\text{eff}} \leq 30 \times \text{pixel size}$; spheroid Sérsic index n : $1 \leq n \leq 5$. Also, for the spheroid-disk fit, we force the disk to be larger than the spheroid and more elliptical. Likewise, for the spheroid-disk-bar fit, we force the disk to be larger than the bar and the spheroid, and the spheroid component to be the most round one of three components.

After running various trials, the two main challenges that we encountered were (i) determining the best values for the PSO chains, to make sure the code converged

¹ <https://github.com/sibirrer/lenstronomy>

² <https://github.com/sibirrer/AstroObjectAnalyser>

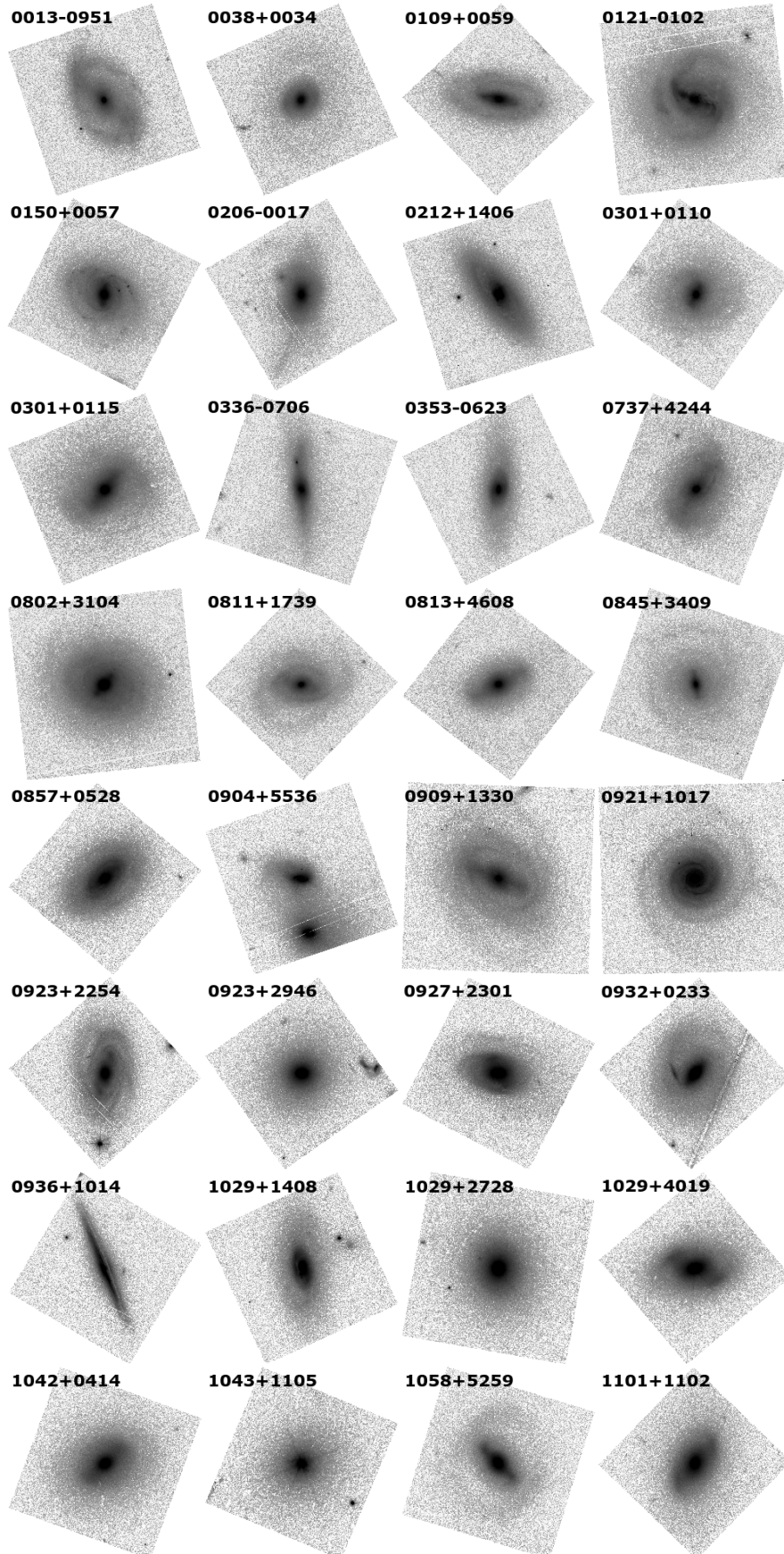


Figure 1. HST UVIS/F814W images of our sample. Cutouts are shown as used for the fitting, but rotated here (North up and East to the left) for display purposes. Image sizes are listed in table 1. Thanks to the high spatial resolution and S/N data, the wide variety of host-galaxy morphologies can clearly be seen.

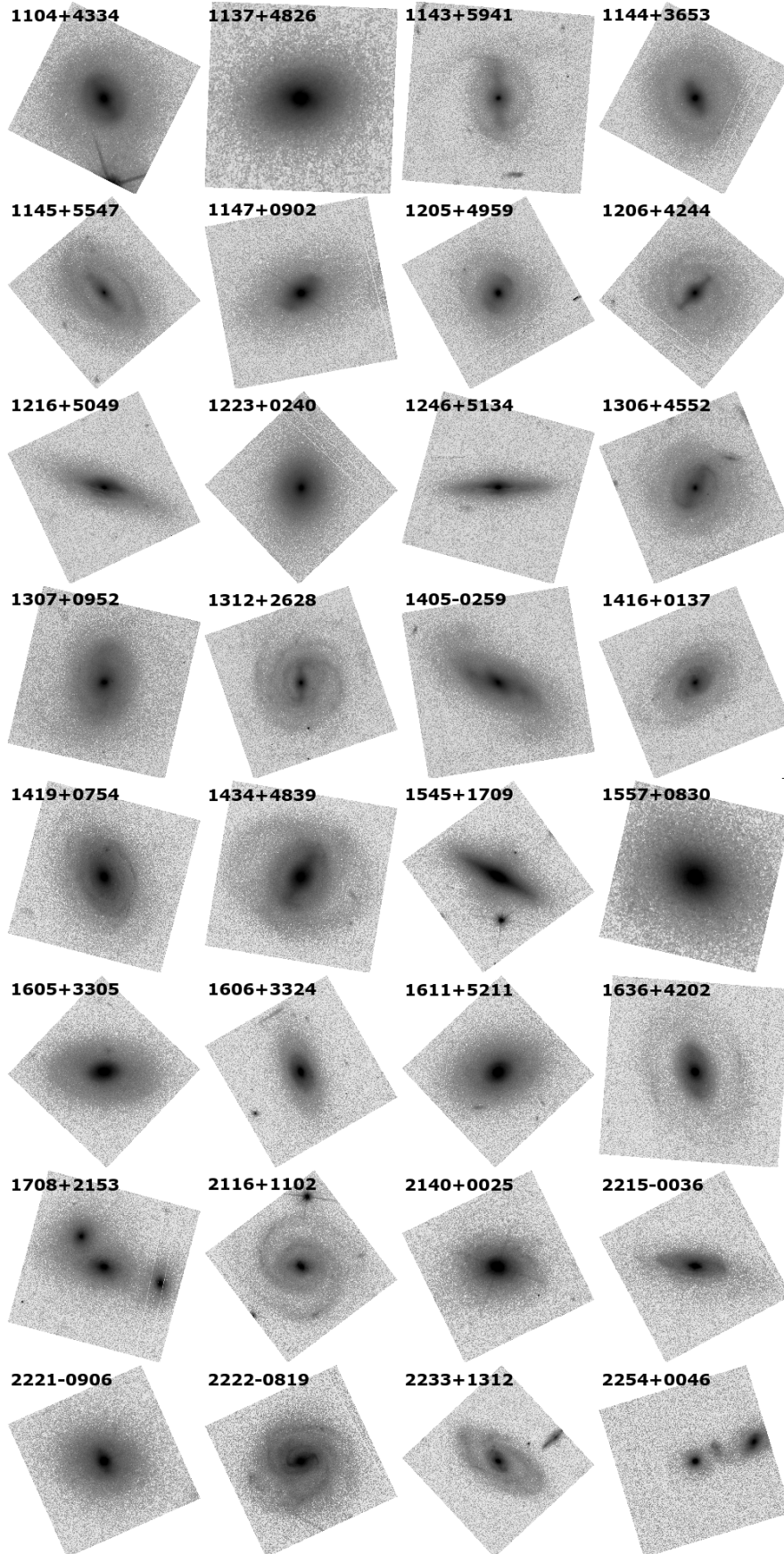


Figure 2. Continuation of Figure 1.

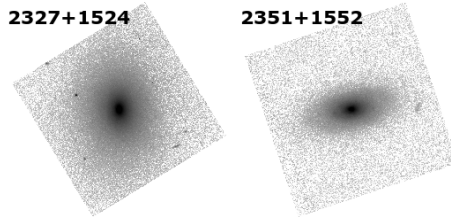


Figure 3. Continuation of Figure 1.

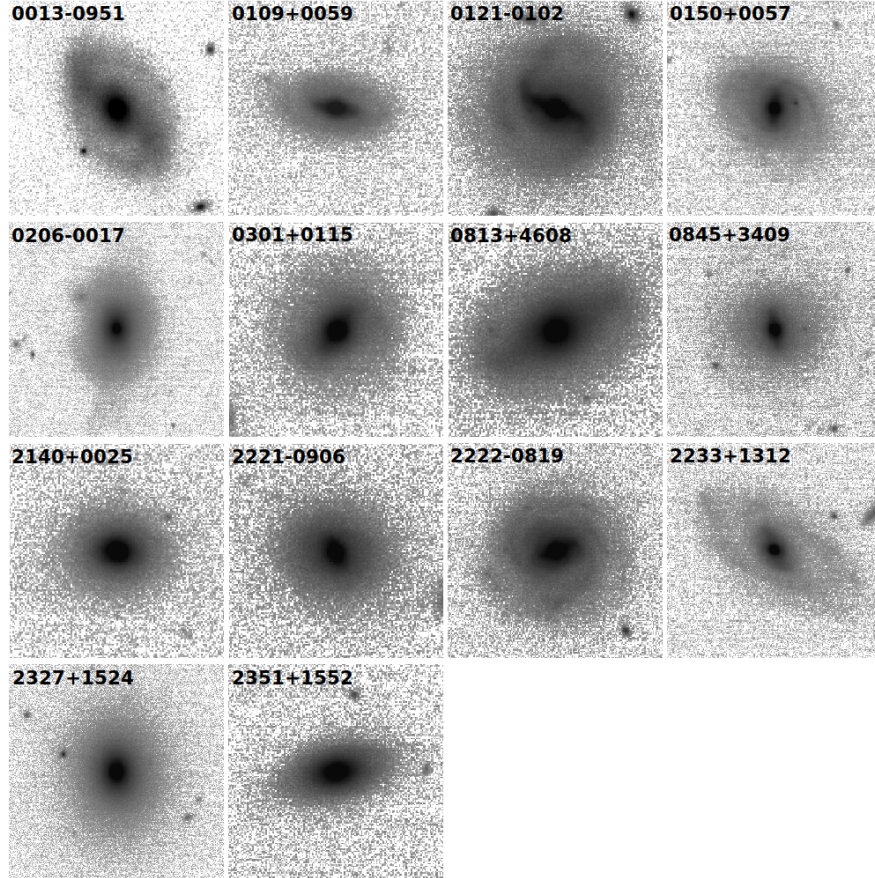


Figure 4. Gemini NIRI Ks images for 14 galaxies. North is up, East is to the left. Image sizes are listed in table 2.

and (ii) making sure that the code converged to the true global minimum and not to a local one. The latter may depend on the starting parameters used, especially if more than one component is fitted to the host galaxy, due to degeneracies involved and the high-dimensional parameter volume. After some experimenting, the following procedure was shown to be successful. We chose a PSO chain that guaranteed convergence even for the largest image size. For a spheroid-only fit, we chose a PSO with 200 particles and 70 iterations, for spheroid-disk and spheroid-disk-bar, a PSO with 300 particles and 100 iterations. For all fits, as a diagnostic, we displayed the log (likelihood) of the fit, particle position and parameter velocity for the different parameters as

a function of iteration to ensure that the chain indeed converged.

First, we ran the spheroid-only fit which was shown to be robust, i.e. giving the same fitting result, regardless of starting parameters used. We then used the results from the spheroid-only fit as starting parameters for the disk in the subsequent spheroid-disk and spheroid-disk-bar fit. For objects for which there is at least an indication of a visual bar, the bar parameters size, position angle and ellipticity were carefully determined manually and used as starting parameters for the bar in the spheroid-disk-bar fit. For both the spheroid-disk and spheroid-disk-bar fit, we chose three different starting parameters for the size of the spheroid and the disk, to

Table 2. Gemini Observations.

Object	Date of Obs.	Exp. time	FWHM	Frame size
	(UT)	(s)	($''$)	($''$)
(1)	(2)	(3)	(4)	(5)
0013–0951	2016 Oct 25	378	0.31	21.1
0109+0059	2016 Oct 14	360	0.32	18.7
0121–0102	2016 Sep 06	360	0.35	23.4
0150+0057	2017 Jan 09	216	0.27	23.4
0206–0017	2017 Jan 09	144	0.24	46.8
0301+0115	2016 Nov 06	360	0.36	16.4
0813+4608	2016 Oct 20	360	0.30	15.2
0845+3409	2016 Oct 30	324	0.40	28.1
2140+0025	2016 July 16	360	0.29	16.4
2221–0906	2016 July 16	540	0.32	16.4
2222–0819	2016 Sep 08	378	0.27	21.1
2233+1312	2016 Aug 7	216	0.32	25.7
2327+1524	2016 Aug 8	216	0.44	35.1
2351+1552	2016 Oct 15	432	0.26	18.7

NOTE— Col. (1): Target ID used throughout the text (based on R.A. and declination). Col. (2): Date of observation (UT). Col. (3): Total exposure time in seconds. Col. (4): Full-Width at Half Maximum (FWHM) of PSF star in arcsecond. Col. (5): Frame size of image shown in Fig. 4 (in arcsecond, in x and y).

cover a broader range. For the spheroid effective radius, we chose three different starting parameters: (i) pixel size * 4, (ii) pixel size * 8, and (iii) pixel size *30. For the disk effective radius we chose these three different starting parameters: (i) spheroid effective radius from spheroid-only fit, (ii) twice the size used in (i), and (iii) half the size used in (i). When combined, this yields nine different starting parameters for both the spheroid-disk and spheroid-disk-bar fits. The nine fits were compared in terms of image residuals and resulting chi-squared values. In most cases, the nine different fits yielded identical results, showing the convergence to a true global minimum. Occasionally, outliers were identified through higher chi-square values and/or from the residual image and excluded. By careful inspection of the images and final fitting results, we determined the best model and fit for all objects. A disk and bar were included in the host-galaxy fitting only if they were clearly visible in the image and/or if their inclusion significantly improved the fit (as evidenced by chi square and residuals), beyond the typical scatter of values seen for the nine different fits for a given model. We conservatively adopt 0.04 dex as uncertainty on the derived luminosities. Figure 5 shows example fits by lenstronomy with our chosen procedure. Table 3 lists all the derived quantities. Table 5 in the appendix gives the details of the fitting parameters.

Galactic foreground extinction was subtracted based on dust reddening measurements from Schlafly & Finkbeiner (2011), assuming $F814W = 0.61 A_V$. Magnitudes were converted to luminosities, applying a k -correction using PySynphot³ (Lim et al. 2015) and a Kinney et al. (1996) Sa galaxy template. Note that given the low redshift of our galaxies, using a different template does not significantly change our results. Also, PySynphot gave (V-I) colors less than 1.2 magnitude for all galaxy templates (elliptical, S0, Sa, or Sb) and thus, the F814W filter magnitudes can be considered identical to I-band magnitudes (Harris 2018).

To derive colors, we fitted the Gemini and SDSS images (in the filters g' , r' , i' and z') in a similar way using lenstronomy. We first used the Gemini images to independently determine the host-galaxy morphology of each galaxy, based on both visual inspection of the images and lenstronomy fitting results. The conclusions reached are identical to those from the HST fitting. We then adopted the same host-galaxy parameters derived from the fitting of the HST images and used lenstronomy to fit the Gemini and SDSS images, leaving only the magnitudes of PSF and host-galaxy components as free parameters. This gives us magnitudes in 5 or 6

³ <https://pysynphot.readthedocs.io/en/latest/>

different filters for the different host-galaxy components spheroid, (pseudo-) bulge, and disk, if present. Dust extinction and k correction were applied.

As many literature studies rely on GALFIT, we also ran GALFIT on the same background-subtracted HST images for comparison, using the same PSFs, error image and general procedure as for lenstronomy. Overall, the results agree, especially (and not surprisingly) for all derived values (magnitudes, effective radius and Sérsic index) for a single-component fit (spheroid only) and magnitudes, independent of fit used (spheroid, spheroid-disk or spheroid-disk-bar) (similar conclusions were also reached by [Yang et al. 2021](#)). The mean of the ratio between magnitudes as determined from lenstronomy and GALFIT is 1.00 ± 0.01 for spheroid magnitude in a spheroid-only fit; 1.00 ± 0.03 for spheroid and 1.01 ± 0.02 for disk in a spheroid-disk fit, and 1.02 ± 0.04 for spheroid, 1.00 ± 0.06 for disk and 1.01 ± 0.01 for bar in a spheroid-disk-bar fit. However, for more complicated models, the effective radii for individual objects

scatter, but the biggest difference is seen in the spheroid Sérsic index (since disk and bar have fixed Sérsic indices) (Fig. 7). While the mean of the ratio between Sérsic index n as determined from lenstronomy and GALFIT is still around 1, it scatters greatly (0.97 ± 0.6 for spheroid-disk fit and 0.97 ± 0.87 for spheroid-disk-bar fit). This cautions the usage of n alone as an indication of the nature of the spheroid (classical vs. pseudo-bulge) and in this paper, we use a conservative approach (see discussion in Section 4.1). However, based on our experience using GALFIT in many previous studies (e.g., [Bennert et al. 2010, 2011a](#)) we want to stress that GALFIT tends to need more user interaction and visual inspections of results to ensure a true global minimum was reached which we did not do here. Lenstronomy’s design of semi-linear inversion and PSO resulted in a significant improvement in automation and reduction of labor-intensive work in the fitting process relative to GALFIT.

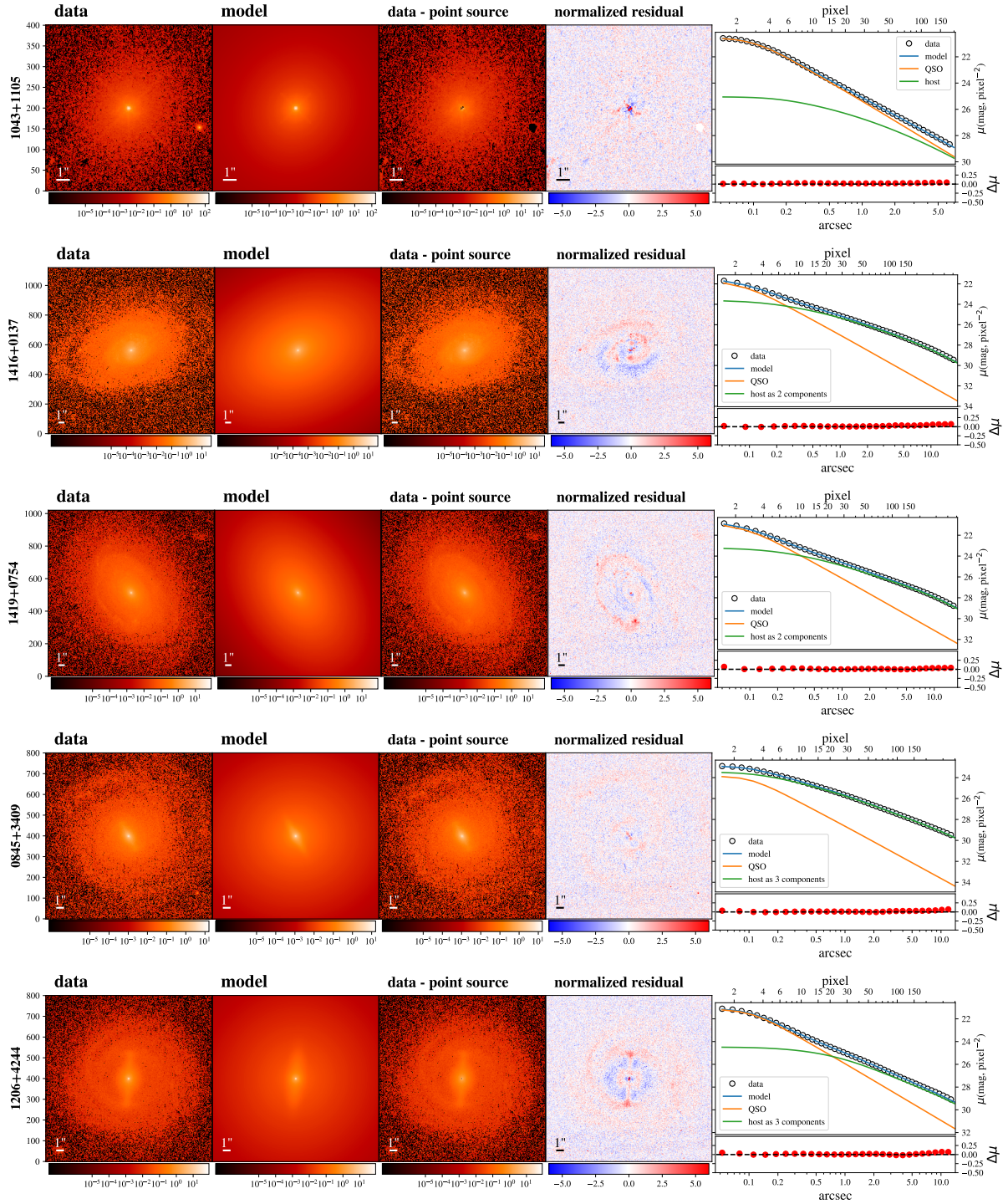


Figure 5. Example fits from lenstronomy. From left to right: HST image (“data”), best fit model derived from lenstronomy (“model”); PSF-subtracted image (“data - Point Source”); residual image after subtraction of best fit model from data, divided by the noise level (“normalized residual”); and surface-brightness profile showing the data as black circles, the model as a blue line, the PSF fitting the central AGN as an orange line and the host-galaxy total fit as a green line. Note that the images are shown as observed with HST and as fitted by lenstronomy, and as such have random orientation (not rotated with North up and East to the left). From top to bottom, five different objects are shown, representing a variety of host-galaxy morphologies: 1043+1105 is an elliptical galaxy fit with a single Sérsic; 1416+0137 is a disk galaxy with classical bulge; 1419+0754 is a disk galaxy with pseudo-bulge; 0845+3409 is a barred disk galaxy with classical bulge; and 1206+4244 is a barred disk galaxy with pseudo-bulge. (Note that the surface-brightness plots in the right panels are shown only for illustrative purposes; the fit was performed on the 2D image. Surface-brightness values are given in the plane of the sky; the x-axis is based on a circularized radius.)

Table 3. Derived quantities

Object	M_{BH} ($\log M_{\odot}$)	σ_{\star} (km s^{-1})	$L_{\text{I, sph}}$ ($\log M_{\odot}$)	$L_{\text{I, sph+bar}}$ ($\log L_{\odot}$)	$L_{\text{I, host}}$ ($\log L_{\odot}$)	$M_{\text{sph, dyn}}$ ($\log M_{\odot}$)	$M_{\text{sph, } \star}$ ($\log M_{\odot}$)	$M_{\text{sph+bar, } \star}$	$M_{\text{host, } \star}$	Host
(1)	(2)	(3)	(4)	(5)	(6)	(7)	(8)	(9)	(10)	(11)
0013-0951	8.11	109	9.48	...	10.38	9.55	9.89 \pm 0.04	...	10.59 \pm 0.16	BD (C)
0038+0034	8.49	120	10.38	...	10.44	10.56	10.43 \pm 0.2	...	10.54 \pm 0.18	BD (C)
0109+0059	7.78	181	9.73	10.05	10.5	9.9	10.29 \pm 0.01	10.38 \pm 0.04	10.83 \pm 0.14	BDB (P)
0121-0102	8.01	133	9.23	10.02	10.74	9.73	BDB (P)
0150+0057	7.51	192	9.92	10.3	10.88	10.2	10.41 \pm 0.06	10.76 \pm 0.11	11.15 \pm 0.15	BDB (P)
0206-0017	8.26	231	10.75	...	11.01	11.01	11.02 \pm 0.16	...	11.25 \pm 0.17	BD (C)
0212+1406	7.58	175	10.03	10.11	10.66	10.28	10.49 \pm 0.12	10.49 \pm 0.15	10.88 \pm 0.18	BDB (P)
0301+0110	7.61	175	10.06	...	10.24	10.28	10.29 \pm 0.18	... \pm ...	10.33 \pm 0.21	BD (C)
0301+0115	7.81	97	9.66	9.97	10.38	9.33	10.13 \pm 0.17	10.3 \pm 0.19	10.66 \pm 0.2	BDB (P)
0336-0706	7.79	229	10.22	...	10.71	10.71	10.66 \pm 0.13	...	10.94 \pm 0.18	BD (P)
0353-0623	7.76	179	10.0	10.13	10.45	10.48	10.17 \pm 0.18	10.33 \pm 0.17	10.59 \pm 0.17	BDB (C)
0737+4244	7.81	179	10.0	...	10.54	10.48	9.93 \pm 0.04	...	10.72 \pm 0.19	BD (C)
0802+3104	7.69	115	9.4	9.63	10.23	9.32	BDB (P)
0811+1739	7.43	143	9.68	9.94	10.45	9.83	10.18 \pm 0.11	10.35 \pm 0.13	10.64 \pm 0.19	BDB (P)
0813+4608	7.4	124	9.96	10.18	10.38	9.87	10.32 \pm 0.13	10.55 \pm 0.14	10.65 \pm 0.15	BDB (C)
0845+3409	7.63	121	9.99	10.11	10.57	10.15	10.54 \pm 0.1	10.58 \pm 0.12	10.8 \pm 0.15	BDB (C)
0857+0528	7.68	133	9.59	...	10.46	9.73	9.47 \pm 0.18	...	10.55 \pm 0.18	BD (C)
0904+5536	8.03	133	9.68	...	9.95	9.73	9.93 \pm 0.17	...	9.94 \pm 0.21	BD (C)
0909+1330	7.47	133	9.42	9.8	10.46	9.73	9.85 \pm 0.14	10.17 \pm 0.15	10.55 \pm 0.19	BDB (P)
0921+1017	7.71	89	10.04	...	10.56	10.22	10.15 \pm 0.18	...	10.64 \pm 0.2	BD (C)
0923+2254	7.95	89	9.94	10.1	10.63	10.22	10.04 \pm 0.19	10.3 \pm 0.17	10.71 \pm 0.2	BDB (P)
0923+2946	7.82	141	10.49	...	10.49	10.6	10.71 \pm 0.18	...	10.71 \pm 0.18	B (C)
0927+2301	7.2	193	10.02	...	10.66	10.23	10.41 \pm 0.15	...	10.88 \pm 0.18	BD (C)
0932+0233	7.7	126	9.86	...	10.33	9.92	10.23 \pm 0.15	...	10.54 \pm 0.17	BD (C)
0936+1014	7.85	126	9.46	...	10.6	9.92	9.92 \pm 0.08	...	10.83 \pm 0.18	BD (C)
1029+1408	8.12	185	10.53	...	10.66	10.83	10.79 \pm 0.17	...	10.8 \pm 0.18	BD (C)
1029+2728	7.18	125	9.75	...	10.0	9.8	9.99 \pm 0.18	...	10.13 \pm 0.19	BD (C)
1029+4019	7.94	180	9.68	...	10.36	10.09	9.82 \pm 0.07	...	10.52 \pm 0.18	BD (C)
1042+0414	7.4	64	9.51	9.72	10.15	8.87	9.81 \pm 0.06	10.04 \pm 0.13	10.36 \pm 0.17	BDB (P)
1043+1105	8.13	64	9.73	...	9.73	8.87	9.58 \pm 0.22	...	9.58 \pm 0.22	B (C)
1058+5259	7.76	122	9.99	10.23	10.46	9.92	10.21 \pm 0.16	10.44 \pm 0.17	10.59 \pm 0.18	BDB (P)

Table 3 continued

Table 3 (continued)

Object	M_{BH} ($\log M_{\odot}$)	σ_{\star} (kms^{-1})	$L_{1,\text{sph}}$ ($\log M_{\odot}$)	$L_{1,\text{sph}+\text{bar}}$ ($\log L_{\odot}$)	$L_{1,\text{host}}$ ($\log L_{\odot}$)	$M_{\text{sph,dyn}}$ ($\log M_{\odot}$)	$M_{\text{sph},\star}$ ($\log M_{\odot}$)	$M_{\text{sph}+\text{bar},\star}$	$M_{\text{host},\star}$	Host
(1)	(2)	(3)	(4)	(5)	(6)	(7)	(8)	(9)	(10)	(11)
1101+1102	8.37	169	10.03	...	10.28	10.63	10.17 ± 0.19	...	10.43 ± 0.17	BD (C)
1104+4334	7.3	82	10.15	10.19	10.21	10.1	10.21 ± 0.19	10.25 ± 0.2	10.3 ± 0.18	BDB (C)
1137+4826	7.0	150	9.59	...	9.88	9.6	9.81 ± 0.06	...	10.08 ± 0.17	BD (C)
1143+5941	7.77	124	9.7	10.01	10.36	9.81	10.21 ± 0.12	10.38 ± 0.14	10.46 ± 0.19	BDB (C)
1144+3653	7.99	169	9.95	...	10.43	10.26	10.19 ± 0.17	...	10.56 ± 0.19	BD (C)
1145+5547	7.48	169	9.28	9.61	10.49	10.26	9.73 ± 0.13	10.1 ± 0.11	10.61 ± 0.19	BDB (C)
1147+0902	8.65	133	10.41	...	10.47	10.51	10.46 ± 0.21	...	10.52 ± 0.2	BD (C)
1205+4959	8.26	164	10.07	...	10.59	10.19	10.33 ± 0.17	...	10.71 ± 0.19	BD (C)
1206+4244	7.58	164	9.72	10.05	10.56	10.19	9.97 ± 0.16	10.34 ± 0.16	10.69 ± 0.19	BDB (P)
1216+5049	8.32	165	10.07	...	10.39	10.51	10.3 ± 0.17	...	10.59 ± 0.18	BD (C)
1223+0240	7.36	165	9.71	...	10.08	10.51	9.9 ± 0.18	...	10.16 ± 0.2	BD (C)
1246+5134	7.19	105	9.6	...	10.07	9.59	10.08 ± 0.08	...	10.33 ± 0.17	BD (P)
1306+4552	7.42	89	9.2	9.79	10.39	9.22	BDB (P)
1307+0952	7.48	89	9.53	9.59	10.44	9.22	9.88 ± 0.02	9.88 ± 0.15	10.56 ± 0.18	BDB (P)
1312+2628	7.77	89	9.5	9.8	10.54	9.22	9.96 ± 0.02	10.24 ± 0.13	10.57 ± 0.2	BDB (P)
1405-0259	7.3	124	9.65	...	10.44	9.94	10.06 ± 0.13	...	10.64 ± 0.18	BD (C)
1416+0137	7.52	149	10.2	...	10.66	10.41	10.61 ± 0.14	...	10.73 ± 0.19	BD (C)
1419+0754	8.26	214	10.16	...	10.89	10.53	10.61 ± 0.13	...	11.06 ± 0.18	BD (P)
1434+4839	7.92	119	9.71	9.99	10.43	9.8	9.76 ± 0.18	10.13 ± 0.18	10.48 ± 0.2	BDB (P)
1545+1709	8.29	165	10.01	...	10.19	10.42	10.04 ± 0.2	...	10.29 ± 0.18	BD (C)
1557+0830	7.92	165	9.74	...	9.74	10.42	9.71 ± 0.21	...	9.71 ± 0.21	B (C)
1605+3305	8.08	200	9.8	...	10.2	10.29	9.9 ± 0.19	...	10.4 ± 0.17	BD (C)
1606+3324	7.8	162	10.13	...	10.38	10.38	10.46 ± 0.16	...	10.59 ± 0.18	BD (C)
1611+5211	7.93	116	9.98	...	10.22	9.76	10.23 ± 0.16	...	10.38 ± 0.18	BD (C)
1636+4202	8.12	149	10.34	10.38	10.49	10.74	10.44 ± 0.18	10.5 ± 0.18	10.62 ± 0.19	BDB (C)
1708+2153	8.46	167	10.23	...	10.57	10.62	10.62 ± 0.13	...	10.76 ± 0.2	BD (P)
2116+1102	8.25	167	9.92	10.02	10.67	10.62	10.14 ± 0.16	10.32 ± 0.16	10.74 ± 0.19	BDB (P)
2140+0025	7.78	113	10.05	...	10.48	9.82	10.33 ± 0.11	...	10.69 ± 0.15	BD (C)
2215-0036	7.87	113	9.91	...	10.58	9.82	10.04 ± 0.17	...	10.83 ± 0.18	BD (C)
2221-0906	8.03	97	10.0	...	10.38	9.98	10.05 ± 0.15	...	10.66 ± 0.16	BD (C)
2222-0819	7.92	107	9.48	10.0	10.79	9.61	8.29 ± 0.04	10.08 ± 0.22	10.96 ± 0.22	BDB (P)
2233+1312	8.37	207	9.93	10.32	10.87	10.3	10.54 ± 0.06	10.84 ± 0.11	11.16 ± 0.15	BDB (P)
2254+0046	7.63	207	10.1	...	10.36	10.3	10.24 ± 0.12	...	10.51 ± 0.18	BD (C)

Table 3 continued

Table 3 (continued)

Object	M_{BH} ($\log M_{\odot}$)	σ_{*} (km s^{-1})	$L_{\text{I, sph}}$ ($\log M_{\odot}$)	$L_{\text{I, sph+bar}}$ ($\log L_{\odot}$)	$L_{\text{I, host}}$ ($\log L_{\odot}$)	$M_{\text{sph, dyn}}$ ($\log M_{\odot}$)	$M_{\text{sph, *}}$ ($\log M_{\odot}$)	$M_{\text{sph+bar, *}}$	$M_{\text{host, *}}$	Host
(1)	(2)	(3)	(4)	(5)	(6)	(7)	(8)	(9)	(10)	(11)
2327+1524	7.78	261	10.56	...	10.85	10.86	11.01 ± 0.12	...	11.18 ± 0.15	BD (C)
2351+1552	8.34	179	10.28	...	10.61	10.49	10.59 ± 0.13	...	10.91 ± 0.14	BD (C)

NOTE— Col. (1): Target ID used throughout the text (based on R.A. and declination). Col. (2): Logarithm of M_{BH} (solar units) (uncertainty of 0.4 dex). Col. (3): Stellar-velocity dispersion within spheroid effective radius (in km s^{-1}) (uncertainty of 0.04 dex). Col. (4): Logarithm of spheroid I-band luminosity (solar units) (uncertainty of 0.04 dex). Col. (5): Logarithm of spheroid+bar I-band luminosity (solar units) (uncertainty of 0.04 dex). Col. (6): Logarithm of host I-band luminosity (solar units) (uncertainty of 0.04 dex). Col. (7): Logarithm of spheroid dynamical mass (solar units) (uncertainty of 0.1 dex). Col. (8): Logarithm of spheroid stellar mass (solar units). Col. (9): Logarithm of spheroid+bar stellar mass (solar units). Col. (10): Logarithm of host stellar mass (solar units). Col. (11): Host-galaxy fit (B: spheroid only, BD: spheroid+disk, BDB: spheroid+disk+bar). In parentheses: Spheroid component: C = classical bulge; P = pseudo-bulge.

3.2. Stellar-velocity dispersion and black hole mass

In the literature, the observed correlation between M_{BH} and σ is generally considered the tightest and thus most fundamental of the M_{BH} -host-galaxy scaling relations (Tremaine et al. 2002; Beifiori et al. 2012; Saglia et al. 2016; Shankar et al. 2016; van den Bosch 2016; de Nicola et al. 2019). Moreover, it is used to calibrate M_{BH} by matching the M_{BH} - σ relation of RM AGNs to that of quiescent galaxies. Thus, robust measurements of σ are essential. There are several definitions of σ used in the literature, resulting in widely differing measurements depending on aperture size used and host-galaxy morphology (see paper III of this series Bennert et al. 2015), with the most robust being spatially-resolved stellar-velocity dispersions within the effective spheroid radius. Spatially-resolved stellar-velocity dispersions were presented in paper II (Harris et al. 2012) based on our Keck spectra. In paper III (Bennert et al. 2015), we determined σ from spatially-resolved σ measurements integrated within the effective spheroid radius (see equation (1) in paper III; Bennert et al. 2015). However, the effective spheroid radius in paper III was based on surface-photometry of SDSS images. We here repeat the same calculation, now using robust effective spheroid radii from the HST surface photometry. When compared, on average, the σ values are similar (the ones based on HST radii are larger by 1%), but with a large scatter of 10%, and a couple of individual objects having changed by as much as 50%. For 16 objects, the lack of sufficient spatially-resolved σ measurements hindered a robust determination of σ within the effective spheroid radius and they were excluded here. Thus, the M_{BH} - σ relation presented in section 4.2 includes 50 objects.

M_{BH} was determined for the entire sample in Bennert et al. (2015), based on the second moment of the broad $\text{H}\beta$ emission line determined from Keck spectroscopy. The 5100\AA AGN luminosity was used as a proxy for BLR size and combined with the width of $\text{H}\beta$ to estimate M_{BH} as in equation (2) in Bennert et al. (2015). In Bennert et al. (2015), a virial factor of $\log f = 0.71$ was assumed (Park et al. 2012; Woo et al. 2015). However, since this virial factor is based on matching the RM AGN sample to a sample of quiescent galaxies from McConnell et al. (2011), we here derived f independently by matching the M_{BH} - σ relation to that of Kormendy & Ho (2013). To do so, we first fix the slope of the M_{BH} - σ relation to the one from Kormendy & Ho (2013) and then adjust $\log f$ to match the intercept, resulting in $\log f = 0.97$. A wide spread in virial factors ($\log f$ ranging between 0.5 and 1.2) has also been found in previous studies, depending on the choice of different quiescent samples, fitting methods and M_{BH} range (e.g., Park et

al. 2012; Shankar et al. 2019), possibly due to selection effects in the local sample of quiescent black holes.

3.3. Stellar and dynamical masses

From our surface photometry (Section 3.1), we have magnitudes for five to six different bands (HST UVIS/F814W, SDSS g' , r' , i' , z' for all objects plus Gemini NIRI/Ks for 14 objects) for the different host-galaxy components, (pseudo-) bulge, disk, and bar, if present. To estimate stellar masses from colors, we use a Bayesian stellar-mass estimation code with priors on age, metallicity and dust content of the galaxy and error bars on the different magnitudes (Auger et al. 2009). To explore the full parameter space and quantify degeneracies, it uses an MCMC sampler. A Chabrier initial mass function (IMF) was assumed, but later, for comparison with literature, converted to a Kroupa IMF (by adding 0.075 to $\log M$). This gives us stellar masses for the different host-galaxy components of 63 objects; for 3 objects, no robust stellar masses could be determined. Thus, the M_{BH} -stellar-mass relations presented in section 4.2 include 63 objects. (Note that the difference in the stellar-mass estimates based on HST+SDSS vs. HST+SDSS+Gemini is within the uncertainties of the stellar-mass estimates in the HST+SDSS measurements (~ 0.15 - 0.2 dex). In particular, no bias is introduced when adding the Gemini results. However, the uncertainties in the stellar-mass measurements are smaller when the K-band magnitudes are included (Table 3), so we use the K-band magnitudes for the stellar-mass determination when available.)

Given σ within the effective radius as described in the previous section, we can also calculate a dynamical mass:

$$M_{\text{sph,dyn}} = c r_{\text{eff,sph}} \sigma_{\text{ap,ref}}^2 / G \quad (1)$$

with $c = 3$ for comparison with literature (Courteau et al. 2014). Since robust σ measurements within the effective spheroid radius were only obtained for 50 objects, the M_{BH} - $M_{\text{sph,dyn}}$ relation in section 4.2 includes 50 objects.

3.4. Comparison samples

To compare the resulting scaling relations of M_{BH} and σ , luminosity and mass with the literature, we use the sample presented by Kormendy & Ho (2013) as a quiescent galaxy comparison sample, 85 local galaxies with M_{BH} based on dynamical modeling of spatially-resolved kinematics. Their sample consist of 44 elliptical galaxies, 20 spiral and S0 galaxies with classical bulge and 21 spiral and S0 galaxies with pseudo-bulge. Five of the elliptical galaxies are mergers in progress. Pseudo-bulges

and mergers are significant outliers in Kormendy & Ho (2013) and ignored here. For 11 objects, the M_{BH} is considered uncertain and these objects are also ignored. We are thus left with 51 objects total, 32 elliptical galaxies and 19 spiral and S0 galaxies with classical bulges.

The stellar-velocity dispersions are adopted in most cases from Gültekin et al. (2009) and represent effective velocity dispersions within $r_{\text{eff}}/2$ as average of $V^2(r) + \sigma^2(r)$ weighted by $I(r)dr$, thus consistent with the way we derived stellar-velocity dispersions, since the difference between averaging inside r_{eff} and $r_{\text{eff}}/2$ is small (Kormendy & Ho 2013).

Kormendy & Ho (2013) list spheroid magnitudes in Ks and V, and (V-Ks) and (B-V) colors. We use a variety of elliptical and spiral spectral templates from Bruzual & Charlot (2003) and Kinney et al. (1996) and derive a linear least-square fit of the form $(V-I) = \alpha*(B-V) + \beta$ with $\alpha = 0.72$ and $\beta = 0.41$, for conversion to I-band magnitudes.

The stellar spheroid masses given by Kormendy & Ho (2013) are derived from a mean of mass-to-light ratios based on σ and $(B-V)_0$ (their equations 8 and 9) and K-band magnitude. The mass-to-light ratio based on color is derived from Into & Portinari (2013), who assume a Kroupa (2001) IMF, but Kormendy & Ho (2013) adjust to the dynamical zeropoint.

For the $M_{\text{BH}}-\sigma$ relation, we also show the 29 RM AGN sample presented by Woo et al. (2015). We adjust their M_{BH} to match the virial factor of $\log f = 0.97$ adopted here.

4. RESULTS AND DISCUSSION

4.1. Host-galaxy morphology

The host-galaxy morphology was determined based on visual inspection of images and the results of the surface-brightness fitting (Section 3.1). Of the full sample of 66 AGNs with HST images, we conclude that 3 are hosted by bona-fide elliptical galaxies and 63 by spiral or S0 galaxies. Out of the latter, 26 galaxies are found to have a bar. Four objects show signs of interaction and/or merger activity (0206–0017, 0904+5536, 1708+2153, 2254+0046). The distribution of host-galaxy morphologies is typical for Seyfert-type AGNs.

In order for a spheroidal component to be classified as pseudo-bulge, we conservatively require that at least three of the following four criteria are met (following Kormendy & Ho 2013): (i) Sérsic index < 2 ; (ii) bulge-to-total luminosity ratio < 0.5 ; (iii) rotation dominated, i.e., ratio between maximum rotational velocity at effective spheroid radius and central stellar-velocity dispersion > 1 ; (iv) for face-on galaxies, the presence of

a bar is considered an indicator for the existence of a pseudo-bulge.

Table 1 gives the host galaxy classification for all objects, including whether or not the above four criteria are met. Kormendy & Ho (2013) argue that if the bulge-to-total luminosity ratio is > 0.5 , the bulge can be considered a classical bulge. As can be seen from the table, all objects that have a bulge-to-total luminosity ratio > 0.5 were indeed classified as a classical bulge, based on our conservative requirement above.

In this way, of the 63 spiral or S0 galaxies, 22 spheroids are classified as pseudo-bulges, the majority of which (19) are in barred spiral galaxies. Given the wide range of host-galaxy morphologies (with mass-to-light ratios ranging between 0.7 and 2.2) and the high quality of the imaging, our sample is ideal to study dependency of the M_{BH} -host-galaxy scaling relations with other parameters such as (pseudo) bulges and bars.

Note that this classification is conservative and may underestimate the true fraction of pseudo-bulges: for face-on galaxies, the true rotation cannot be reliably measured, for edge-on galaxies, bars can easily be missed. To estimate the fraction of potentially mis-classified bulges (classical instead of pseudo-bulge), we carefully inspected all images. We consider ten galaxies (0013-0951, 0038+0034, 0121-0102, 0150+0057, 0301+0110, 0921+1017, 1205+4959, 1312+2628, 2116+1102, 2222-0819) as face-on (or close to face-on) galaxies. Out of these, five galaxies are already classified as pseudo-bulges based on meeting three of the four criteria (0121-0102, 0150+0057, 1312+2628, 2116+1102, and 2222-0819). For four galaxies, either no criterion is met (0038+0034) or only one criterion (0301+0110, 0921+1017, 1205+4959), so their classifications as classical bulge is independent of criterion (iii). There is only one object (0013-0951) that meets two criteria, but does not seem rotation-dominated and this could indeed be a pseudo-bulge. As for highly-inclined galaxies, there are six we consider in more detail (0336-0706, 0936+1014, 1216+5049, 1246+5134, 1545+1709, 2215-0036). One already meets three criteria (1246+5134) and is already classified as a pseudo-bulge. Two other objects either meet no criterion (1545+1709) or only meet one criterion (1216+5049). That leaves three objects that may potentially be mis-classified as classical bulges (0336-0706, 0936+1014, 2215-0036). Thus, the number of pseudo-bulges in the sample can be considered a lower limit. However, as we discuss in the next section, there are no outliers (whether pseudo-bulge or classical bulge) in the scaling relations, so the conclusions remain unchanged.

4.2. *Scaling relations*

We present scaling relations between M_{BH} and stellar velocity dispersion σ (within effective radius of spheroid), dynamical spheroid mass, stellar mass, and I-band luminosity (Figure 6). We choose Kormendy & Ho (2013) for a consistent comparison for all these different scaling relations, even though there are more recent studies with a compilation of larger samples. However, in a review by Greene et al. (2020), the authors note that their results on the $M_{\text{BH}}-\sigma$ relation would not have changed if, instead of using a recent literature compilation, they had used exclusively the Kormendy & Ho (2013) sample. For the $M_{\text{BH}}-\sigma$ relation, we also show 29 RM AGNs measured in a similar way (Woo et al. 2015, see Section 3.4 for details).

Following common practices, we fit the different scaling relations as the linear relation with α and β as slope and intercept values (Table 4). The error bars of the measurements (in both x and y) are taken into account to perform the inference. We first use SciPy (Virtanen et al. 2020) to estimate the minimization of these parameters. Then, we use the minimization results as initial values to run MCMC (using the EMCEE package Foreman-Mackey et al. 2013). After burn-in, the MCMC chain median values are adopted as the ‘best-fit’ values which are presented in the paper. The upper and lower limits are the 84% and 16% of the chain histogram, respectively. The intrinsic scatter is estimated so that when the squares of the observed uncertainties are summed up, the best-fit reduced chi-square value is close to unity. We fit all samples (including RM AGNs and quiescent galaxies) using the same code, for consistency, rather than using literature values. However, none of our conclusions would change if we were to use the fits given in the literature instead (Kormendy & Ho 2013; Woo et al. 2015).

For all of the M_{BH} scaling relations, our sample of 66 local AGNs naturally extends the correlations for quiescent galaxies down to $M_{\text{BH}} \sim 10^7 M_{\odot}$ along the same line, with the same slope and normalization. However, by itself, the dynamic range in M_{BH} covered by our sample is too small to determine the slope. Thus, when deriving fits to the different scaling relations, we either fit both samples (AGNs and quiescent galaxies) together or when fitting our AGN sample alone, we fix the slope to that of Kormendy & Ho (2013).

The $M_{\text{BH}}-\sigma$ relation of our local AGN sample with M_{BH} determined using the single-epoch method and σ based on spatially-resolved kinematics agrees with that of AGNs with M_{BH} obtained from reverberation mapping (Park et al. 2012; Woo et al. 2015). The importance of the RM AGN sample cannot be overstated since it

serves as the M_{BH} calibrator beyond the local Universe. Given that, within the uncertainties, slope and scatter of the $M_{\text{BH}}-\sigma$ relation of our local AGNs, selected based solely on broad $\text{H}\beta$ emission line width, agree with that of RM AGNs provides a confirmation that the selection of the RM AGN sample based on variability (not on well defined galaxy/black-hole mass properties) does not introduce biases. Moreover, the close agreement between both samples provides an indirect validation of the single-epoch method for the estimation of M_{BH} . (Note that these conclusions are independent of the fact that the $M_{\text{BH}}-\sigma$ scaling relation of our local AGNs is matched to that of inactive galaxies, since that only affects the normalization, but not slope and scatter. Moreover, we do not determine a virial factor for the RM AGNs separately, but use the same one as for our local AGNs, resulting in a good agreement, providing an additional check that the two samples match.)

To illustrate the effect of un-identified bars, we also include scaling relations for stellar mass and luminosity with spheroid+bar component added. This may help in comparison with literature data, especially given the difficulties and potential ambiguities involved in decomposition of images with poor data quality. Since the spheroids in the majority of barred spiral galaxies in our sample are classified as pseudo-bulges (19/26), this affects the location of pseudo-bulges the most. It moves the pseudo-bulges further to the right in the M_{BH} -stellar mass and M_{BH} -luminosity relations which tends to move them into better agreement with the scaling relations of quiescent galaxies. However, within the uncertainty, the difference is small. For none of the scaling relations do we find a significant difference between pseudo- and classical bulges in terms of correlations with M_{BH} . This is in line with some studies (e.g., Davis et al. 2018), but contrary to many others (e.g., Hu 2008; Greene et al. 2010; Sani et al. 2011; Läscher et al. 2016; Saglia et al. 2016; Menci et al. 2016; de Nicola et al. 2019). For example, Kormendy & Ho (2013) went so far to conclude that “any M_{BH} correlations with the properties of disk-grown pseudobulges [...] are weak enough to imply no close coevolution” (see also, Kormendy et al. 2011).

Pseudo-bulges, considered to have evolved secularly through dissipative processes rather than through galaxy mergers (e.g., Courteau et al. 1996; Kormendy & Kennicutt 2004), play an important role for understanding the origin of the M_{BH} scaling relations. If major mergers are the fundamental drivers of the M_{BH} scaling relations, only classical bulges, centrally concentrated, mostly red and quiescent, merger-induced systems, should follow these tight correlations. On the basis of high-quality HST imaging, a careful analysis and

a conservative classification of bulges as pseudo-bulges, our results clearly show that pseudo-bulges follow the same relations as classical bulges, confirming findings of an earlier study of ours based on SDSS images (Bennert et al. 2011a). This is in line with studies that argue that most of the growth of the SMBH happens gradually over time via secular processes (e.g., Simmons et al. 2017; Martin et al. 2018). (Note that none of our results would change if we excluded the pseudo-bulges from our sample, to more closely match the comparison sample by Kormendy & Ho (2013) for which we excluded pseudo-bulges. While our sample consists of a significant fraction of pseudo-bulges (22 of 66 galaxies), when repeating all the fits presented in Table 4 without pseudo-bulges, we obtain fits with the same parameters within the uncertainties. This is not surprising and highlights the fact that pseudo-bulges do not form outliers in our sample.)

In fact, our study shows that there are no significant outliers that could be attributed to any specific category, whether it be galaxies with pseudo-bulges, bars or signs of interactions/mergers. For example, the four objects with signs of mergers/interaction do not tend to lie off the relations. Likewise, barred galaxies (26 out of 63 disk galaxies in our sample) do not form outliers, in line with some literature (Beifiori et al. 2012; Sahu et al. 2019). The location of barred galaxies on the scaling relations is not only important since over half of the disk galaxy population is barred (e.g., Weinzirl et al. 2009), but also because of the relevance of bars in secular evolution and potentially fueling of BHs. Moreover, it is much easier to identify a bar than a pseudo-bulge (for a discussion, see Graham 2016), a reason why some studies choose to distinguish between barred and non-barred galaxies rather than classical vs. pseudo-bulges (e.g., Graham & Scott 2013). Most previous literature studies found barred galaxies to lie off the M_{BH} scaling relations, in particular in the case of $M_{\text{BH}}-\sigma$ (e.g., Graham 2008; Graham & Li 2009; Hu 2008, for conflicting results, see also Beifiori et al. 2012). This is not surprising, given that the stellar dynamics in galactic sub-structures such as bars and pseudo-bulges is very different from that of elliptical galaxies or classical bulges. Moreover, σ measurements can depend significantly on, e.g., size of the fiber (as is the case, for example, for SDSS), orientation of the slit (in case of long-slit observations) and aperture size used (for details and comparisons, see Bennert et al. 2015). Integral-field spectroscopy and spatially-resolved spectroscopy is an obvious step forward and has been obtained for a sub-sample of the RM AGN sample (Batiste et al. 2017). While our σ measurements were obtained using long-slit spectroscopy, we mitigate these effects by

using spatially-resolved measurements integrated within the spheroid effective radius which is a robust way to determine σ (see also Bennert et al. 2015). (Note that while we may be underestimating the true fraction of barred galaxies in our sample, given they are hard to identify in edge-on galaxies (see Section 4.1), this does not affect our conclusions, since there are no outliers (barred or not) in the scaling relations.)

The majority of AGNs in our sample reside in host galaxies of S0 or late-type morphology (63/66), out of which almost half of the galaxies are barred and a third of spheroids are classified as pseudo-bulges. The fact that all of them are obeying the same tight M_{BH} scaling relations, highlights the importance of secular evolution for the growth of BHs and bulges. Secular evolution may have a synchronizing effect, growing BHs and bulges simultaneously at a small but steady rate for late-type galaxies, and keeping them on tight relations over time. Comparison with semi-analytical models for galaxy formation including secular evolution (such as e.g., Menci et al. 2016, who, however, find little or no correlation of pseudo-bulge mass with M_{BH}) can further shed light on such a scenario, but is beyond the scope of this paper.

The $M_{\text{BH}}-\sigma$ relation is considered the most fundamental of the scaling relations, due to its tightness (0.3 dex in $\log M_{\text{BH}}$) (Tremaine et al. 2002; Beifiori et al. 2012; Saglia et al. 2016; van den Bosch 2016; de Nicola et al. 2019), or based on residuals and principle-component analyses (Shankar et al. 2016; Marsden et al. 2021), at least for late-type spiral galaxies (Gültekin et al. 2009; Greene et al. 2010; Läscher et al. 2016, see, however, Davis et al. 2019). Interestingly, we do not find significant differences in the tightness of the different correlations. The scatter in the relations ranges between 0.2-0.4 dex, smaller or equal to that of quiescent galaxies (Gültekin et al. 2009; McConnell & Ma 2013; Kormendy & Ho 2013). (Note that even though the quiescent galaxies span a larger range in M_{BH} , we can still compare the scatter between the different samples, assuming that the scatter is independent of M_{BH} .) We attribute this difference to a combination of (i) our homogeneous sample selection, (ii) high-quality data, for both imaging and spectroscopy, and (iii) reliable surface photometry for a detailed structural decomposition of the host galaxy components and spatially-resolved kinematics. Given the fact that the biggest uncertainty in host-galaxy surface-brightness fitting is the classification and identification of individual structures, a combination of (ii) and (iii) is essential if one wants to determine the role of host-galaxy sub-structures on the correlation with M_{BH} .

5. SUMMARY

This paper presents a study of 66 local ($0.02 \leq z \leq 0.1$) active galactic nuclei (AGNs) homogeneously selected based on the presence of a broad $H\beta$ emission line in SDSS spectra. High-quality HST optical (66 objects) and Gemini NIR imaging (14 of 66 objects) are complemented by spatially-resolved kinematics from spectra obtained at the Keck Telescopes. M_{BH} is determined based on the single-epoch method with broad $H\beta$ emission-line width measured from Keck spectra. Surface photometry is performed using state of the art methods, providing a structural decomposition of the AGN host galaxies into spheroid, disk and bar (when present), with the spheroid component conservatively being classified as either classical or pseudo-bulge. Scaling relations between M_{BH} -and host galaxy properties — spatially-resolved stellar-velocity dispersion, dynamical spheroid mass, stellar spheroid mass and spheroid luminosity — are presented, in comparison with quiescent galaxies and RM AGNs taken from the literature. Our findings can be summarized as follows:

1. The majority of AGNs (63/66) are hosted by galaxies classified as spiral or S0 with a high fraction of bars (26/63) and pseudo-bulges (22/63), typical for Seyfert-type galaxies. The wide variety of host-galaxy morphologies makes our sample ideally suited to study the dependency of the M_{BH} -host-galaxy scaling relations with other parameters such as (pseudo) bulges and bars.
2. Tight correlations are found between M_{BH} and spatially-resolved stellar-velocity dispersion, dynamical spheroid mass, stellar spheroid mass and spheroid luminosity, without significant differences in the scatter. This is contrary to the widely accepted paradigm that the $M_{\text{BH}}-\sigma$ relation is the most fundamental of all scaling relations.
3. The intrinsic scatter of 0.2-0.4 dex is smaller than or comparable to that of quiescent galaxies, showing that spiral galaxies hosting AGNs follow the same tight M_{BH} scaling relations, contrary to many literature studies.
4. We do not find any particular outliers: objects with bars, pseudo-bulges or signs of merger activity all fall within the intrinsic scatter of the relations. Our results rule out hierarchical assembly as the sole origin of the M_{BH} -host-galaxy scaling relations and highlight the importance of secular evolution for growing both M_{BH} and spheroid.
5. Within the uncertainties, the $M_{\text{BH}}-\sigma$ relation of our AGNs is indistinguishable from the relation of AGNs with M_{BH} obtained through reverberation mapping. This indirectly validates single-epoch virial estimators of M_{BH} and is consistent with no significant selection bias for RM AGNs.

Our results show that all the tight correlations can be simultaneously satisfied by AGN hosts in the 10^7 - $10^9 M_{\odot}$ regime if data of sufficient quality are in hand and great care is taken when deriving host-galaxy properties. A simple explanation of the difference between our uniformly tight relations and the larger scatter found in the literature is that σ is generally measured more accurately than the other host galaxy parameters. The sample presented in this paper is meant to serve as a local reference point for studies of the cosmic evolution of the correlations between host galaxy properties and M_{BH} .

ACKNOWLEDGEMENTS

We thank the anonymous referee for their thorough report and many valuable comments that helped to improve the paper. We thank Stephane Courteau, Alessandra Lamastra, Michael McDonald, Nicola Menci, Anowar Shajib, Daeseong Park and Jong-Hak Woo for helpful discussions. VNB, IS and TS gratefully acknowledge assistance from National Science Foundation (NSF) Research at Undergraduate Institutions (RUI) grants AST-1312296 and AST-1909297. Note that findings and conclusions do not necessarily represent views of the NSF. TT acknowledges support by NSF through grant AST-1907208, and by the Packard Foundation through a Packard Research Fellowship. IS is supported by the German Research Foundation (DFG, German Research Foundation) under Germany's Excellence Strategy - EXC 2121 "Quantum Universe" - 390833306. Based on observations obtained with the Hubble Space Telescope and supported by a Space Telescope Science Institute (STScI) grant associated with program HST-GO-15215. Support for Program number HST-GO-15215 was provided by NASA through a grant from the Space Telescope Science Institute, which is operated by the Association of Universities for Research in Astronomy, Incorporated, under NASA contract NAS5-26555. VNB also gratefully acknowledges support by NASA grant 80NSSC19K1016. Based on observations obtained at the international Gemini Observatory, a program of NSF's NOIRLab (processed using the Gemini IRAF package), which is managed by the Association of Universities for Research in Astronomy (AURA) under a cooperative agreement with the National Science Foundation on behalf of the Gemini Observatory partnership:

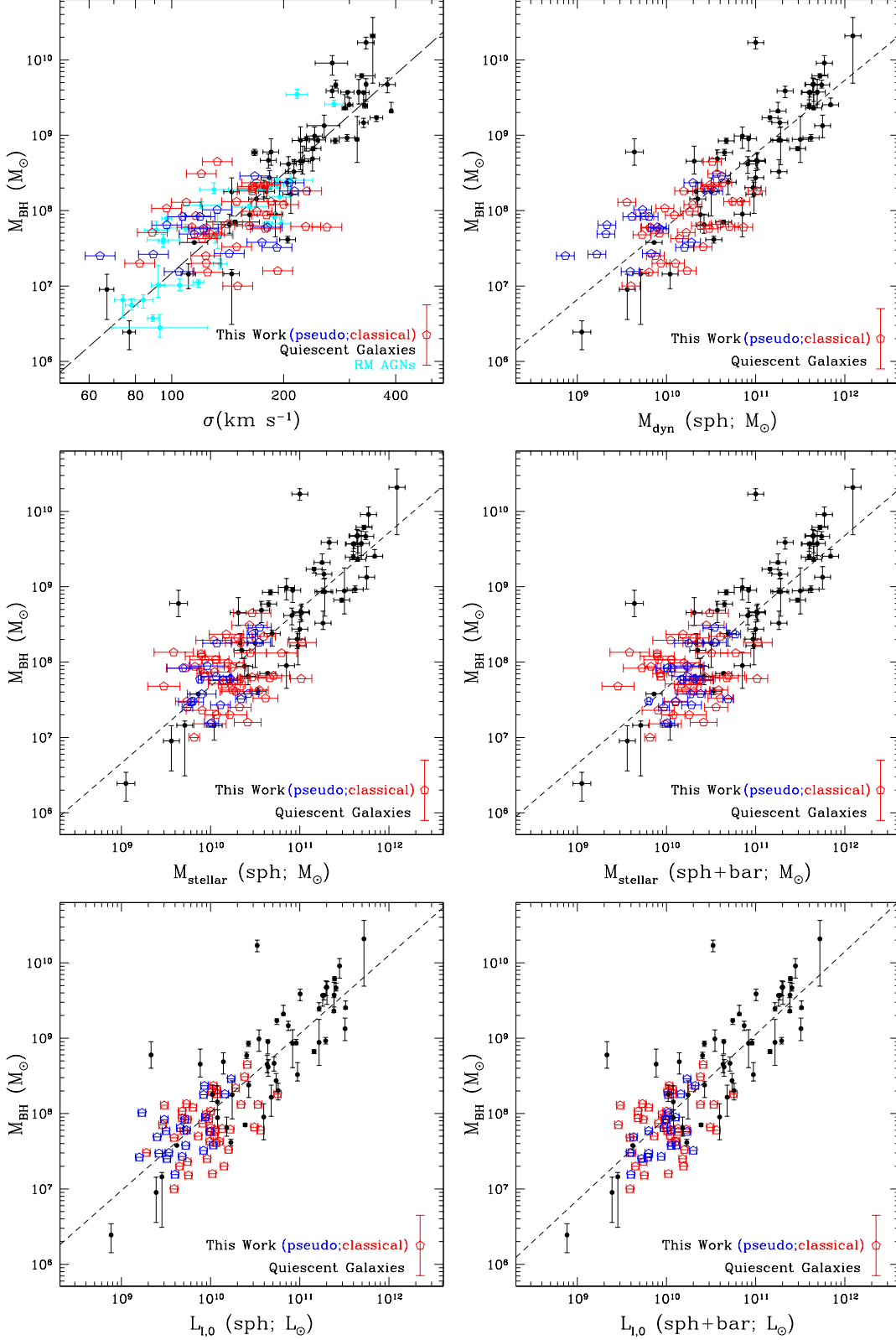


Figure 6. M_{BH} scaling relations. In all panels, black data points correspond to the local quiescent comparison sample from Kormendy & Ho (2013), only including elliptical galaxies and spiral galaxies with classical bulge. For our sample, pseudo-bulges are shown in blue and classical bulges in red. To reduce confusion of data points, error bars on M_{BH} for our sample are omitted and shown instead in the bottom right corner. Top left panel: $M_{\text{BH}}-\sigma$ relation. Cyan data points show 29 RM AGNs from Woo et al. (2015). Top right panel: $M_{\text{BH}}-M_{\text{sph,dyn}}$ relation. Middle left panel: $M_{\text{BH}}-M_{\text{sph}}$ relation. Middle right panel: $M_{\text{BH}}-M_{\text{sph+bar}}$ relation. Bottom left panel: $M_{\text{BH}}-L_{\text{sph,I}}$ relation. Bottom right panel: $M_{\text{BH}}-L_{\text{sph+bar,I}}$ relation.

Table 4. Fits to the Local Scaling Relations.

X in relation	Sample	α	β	Scatter
(1)	(2)	(3)	(4)	(5)
$\sigma/200\text{km s}^{-1}$	AGNs (50) & Quiescent galaxies (51)	8.52 ± 0.56	4.00 ± 0.25	0.35 ± 0.04
$\sigma/200\text{km s}^{-1}$	Quiescent galaxies (51)	8.53 ± 0.68	4.55 ± 0.29	0.33 ± 0.04
$\sigma/200\text{km s}^{-1}$	AGNs (50)	8.51 ± 0.08	4.55 (fixed quiescent)	0.42 ± 0.08
$\sigma/200\text{km s}^{-1}$	AGNs (50) & RM AGNs (29) & Quiescent galaxies (51)	8.50 ± 0.46	4.01 ± 0.21	0.37 ± 0.03
$\sigma/200\text{km s}^{-1}$	RM AGNs (29) & Quiescent galaxies (51)	8.54 ± 0.51	4.34 ± 0.23	0.38 ± 0.04
$\sigma/200\text{km s}^{-1}$	RM AGNs (29)	8.45 ± 1.15	3.89 ± 0.53	0.42 ± 0.06
$\sigma/200\text{km s}^{-1}$	RM AGNs (29)	8.57 ± 0.09	4.55 (fixed quiescent)	0.45 ± 0.06
$M_{\text{sph}}/10^{11}M_{\odot}$	Quiescent galaxies (52)	8.78 ± 1.06	1.05 ± 0.1	0.43 ± 0.05
$M_{\text{sph,dyn}}/10^{11}M_{\odot}$	AGNs (50) & Quiescent galaxies (52)	8.76 ± 0.69	0.97 ± 0.06	0.37 ± 0.04
$M_{\text{sph,dyn}}/10^{11}M_{\odot}$	AGNs (50)	8.77 ± 0.07	1.05 (fixed quiescent)	0.14 ± 0.1
$M_{\text{sph,stellar}}/10^{11}M_{\odot}$	AGNs (63) & Quiescent galaxies (52)	8.72 ± 0.7	0.97 ± 0.07	0.39 ± 0.04
$M_{\text{sph+bar,stellar}}/10^{11}M_{\odot}$	AGNs (sph+bar) (63) & Quiescent galaxies (52)	8.71 ± 0.74	1.05 ± 0.07	0.38 ± 0.04
$M_{\text{sph,stellar}}/10^{11}M_{\odot}$	AGNs (63)	8.59 ± 0.06	1.05 (fixed quiescent)	0.12 ± 0.1
$L_{\text{sph,I}}/10^{11}L_{\odot}$	AGNs (66) & Quiescent galaxies (51)	9.06 ± 0.73	1.03 ± 0.07	0.39 ± 0.04
$L_{\text{sph,I}}/10^{11}L_{\odot}$	AGNs (sph+bar) (66) & Quiescent galaxies (51)	9.05 ± 0.76	1.11 ± 0.07	0.40 ± 0.04
$L_{\text{sph,I}}/10^{11}L_{\odot}$	Quiescent galaxies (51)	9.11 ± 1.15	1.02 ± 0.11	0.47 ± 0.06
$L_{\text{sph,I}}/10^{11}L_{\odot}$	AGNs (66)	8.88 ± 0.05	1.02 (fixed quiescent)	0.08 ± 0.07

NOTE— For consistency, all fits were calculated as part of this paper, including those to RM AGNs and quiescent galaxies alone. The relations plotted as dashed lines in Fig. 6 correspond to the ones given in sample “AGN & Quiescent galaxies.” (Note that the small scatter in the $M_{\text{BH}}-L_{\text{sph,I}}$ relation implies that the scatter is dominated by the measurement uncertainties.) Col. (1): Scaling relation of the form $\log(M_{\text{BH}}/M_{\odot}) = \alpha + \beta \log X$ with X given in the table. Col. (2): Sample used for fitting (AGNs = the AGNs in this paper; quiescent = elliptical galaxies and classical bulges from Kormendy & Ho (2013); RM AGNs = AGNs with M_{BH} determined from reverberation-mapping taken from Woo et al. (2015). In parentheses, number of galaxies in each sample are given. Col. (3): Mean and uncertainty of the best fit intercept. Col. (4): Mean and uncertainty of the best fit slope. Col. (5): Mean and uncertainty of the best fit intrinsic scatter.

the National Science Foundation (United States), National Research Council (Canada), Agencia Nacional de Investigación y Desarrollo (Chile), Ministerio de Ciencia, Tecnología e Innovación (Argentina), Ministério da Ciência, Tecnologia, Inovações e Comunicações (Brazil), and Korea Astronomy and Space Science Institute (Republic of Korea). Based on observations obtained at the W. M. Keck Observatory, which is operated as a scientific partnership among Caltech, the University of California, and the National Aeronautics and Space Administration (NASA). The Observatory was made possible by the generous financial support of the W. M. Keck Foundation. The authors recognize and acknowledge the very significant cultural role and reverence that the summit of Mauna Kea has always had within the indigenous Hawaiian community. We are most fortunate to have the opportunity to conduct observations from this mountain. This research has made use of the Dirac computer cluster at the California Polytechnic State University in San Luis Obispo, maintained by Dr. Brian Granger and Dr. Ashley Ringer McDonald, and the Hoffman2 Cluster at the University of California Los Angeles, managed and operated by the IDRE Research Technology Group under the direction of Lisa Snyder. This research has made use of the public archive of the

Sloan Digital Sky Survey (SDSS) and the NASA/IPAC Extragalactic Database (NED) which is operated by the Jet Propulsion Laboratory, California Institute of Technology, under contract with the National Aeronautics and Space Administration. This research has made use of the NASA/IPAC Infrared Science Archive, which is funded by the National Aeronautics and Space Administration and operated by the California Institute of Technology. We thank Gemini staff observers K. Chibocas, W. Fraser, L. Fuhrmann, T. Geballe, M. Hoenic, J. Miller, S. Pakzad, R. Pike, M. Schwamb, O. Smirnova, and A. Smith for obtaining these data in queue mode.

Facilities: HST (WFC3), Keck:I (LRIS), Gemini:Gillett (NIRI), Sloan

Software: astropy (Astropy Collaboration 2013) EMCEE (Foreman-Mackey et al. 2013) GALFIT (Peng et al. 2002), IRAF (Tody 1986, 1993), L.A. Cosmic (van Dokkum 2001), lenstronomy (Birrer et al. 2018), Matplotlib (Hunter 2007) Particle Swarm Optimizer (Kennedy & Eberhart 2001), photutils (Bradley et al. 2016), PyRAF (Science Software Branch at STScI 2012), PySynphot (Lim et al. 2015), Python libraries (Van Rossum 2009), SciPy (Virtanen et al. 2020)

APPENDIX

Table 5. Surface-Photometry Fitting Results.

Object	HST <i>I</i> -band			Gemini <i>K_s</i> -band			HST											
	AGN (mag)	Spheroid (mag)	Disk (mag)	Bar (mag)	AGN (mag)	Spheroid (mag)	Disk (mag)	Bar (mag)	η_{sph} (10)	R_{sph} (μ)	PA_{sph} (deg)	q_{sph} (13)	R_{disk} (μ)	PA_{disk} (deg)	q_{disk} (16)	R_{bar} (μ)	PA_{bar} (deg)	q_{bar} (19)
(1)	(2)	(3)	(4)	(5)	(6)	(7)	(8)	(9)	(10)	(11)	(12)	(13)	(14)	(15)	(16)	(17)	(18)	(19)
0013-0951	18.3	18.0	15.9	...	16.0	17.5	15.0	...	1.2	0.36	12.6	0.77	5.19	39.2	0.52
0038+0034	17.9	16.3	18.3	4.5	2.39	158.0	0.82	2.39	104.9	0.44
0109+0059	18.9	18.3	16.9	18.2	17.8	17.1	15.9	17.2	1.6	0.2	74.8	0.63	3.2	80.2	0.53	1.11	78.2	0.31
0121-0102	16.7	18.4	14.8	16.6	15.1	17.0	14.1	15.6	1.0	0.42	33.6	0.95	5.35	67.1	0.95	2.71	66.6	0.27
0150+0057	19.1	17.6	15.5	17.2	17.0	16.8	14.6	16.2	1.0	0.39	63.9	0.84	3.92	54.8	0.8	1.3	172.0	0.4
0206-0017	19.0	14.1	14.2	...	16.0	13.1	13.5	...	3.8	3.27	1.7	0.72	9.42	174.6	0.56
0212+1406	18.4	16.8	15.6	18.4	1.0	0.75	0.3	0.64	4.22	38.3	0.42	0.37	58.9	0.39
0301+0110	18.1	16.9	17.7	4.0	1.2	162.0	0.65	3.35	77.1	0.65
0301+0115	18.0	18.1	16.8	18.1	15.9	16.4	15.7	17.3	1.0	0.23	88.3	0.89	2.95	118.5	0.77	1.46	145.0	0.34
0336-0706	20.7	17.2	16.4	1.0	0.77	15.6	0.67	5.4	4.1	0.24
0353-0623	18.4	17.3	16.9	18.4	1.0	0.94	159.3	0.73	4.75	177.1	0.34	0.27	179.7	0.34
0737+4244	19.7	17.5	16.6	2.7	0.11	158.3	0.8	2.85	19.2	0.56
0802+3104	17.2	17.4	15.6	17.7	1.1	0.28	66.1	0.85	3.27	74.0	0.84	1.01	140.0	0.4
0811+1739	19.1	17.7	16.2	17.9	1.4	0.38	105.9	0.79	4.48	97.3	0.73	2.88	71.4	0.39
0813+4608	20.1	16.6	16.6	17.0	17.8	15.7	15.7	16.1	2.6	0.67	105.8	0.89	5.14	106.3	0.69	3.58	118.4	0.37
0845+3409	20.1	16.9	15.9	18.1	17.4	15.7	15.2	17.2	3.9	1.09	16.1	0.89	7.0	77.1	0.89	1.66	10.0	0.27
0857+0528	18.0	17.7	15.6	1.2	0.38	131.1	0.71	3.56	133.6	0.59
0904+5536	16.7	16.4	16.6	1.8	1.35	84.7	0.57	7.42	46.2	0.49
0909+1330	20.6	17.7	15.4	17.3	1.5	0.64	38.0	0.88	7.61	45.7	0.75	4.61	70.1	0.24
0921+1017	18.7	15.7	14.7	5.0	3.88	85.6	0.97	3.97	108.1	0.97
0923+2254	16.4	15.5	14.2	16.4	1.4	0.95	173.0	0.79	10.9	176.3	0.56	6.4	160.7	0.25
0923+2946	21.1	15.5	4.8	2.37	111.9	0.91
0927+2301	17.7	14.8	13.5	1.4	1.24	99.0	0.71	7.46	66.4	0.71
0932+0233	18.3	16.9	16.2	1.1	0.68	140.1	0.7	4.37	145.9	0.7
0936+1014	16.9	18.0	15.2	1.4	0.65	19.3	0.33	6.15	23.0	0.31
1029+1408	18.3	15.4	16.6	4.3	2.42	11.8	0.48	5.87	3.2	0.44
1029+2728	19.8	16.2	16.5	3.1	0.78	175.7	0.88	3.21	12.2	0.84
1029+4019	17.4	17.7	16.2	1.1	0.42	109.2	0.64	2.5	84.1	0.64
1042+0414	18.8	17.6	16.5	18.1	1.6	0.25	114.0	0.85	3.21	117.6	0.79	2.02	134.8	0.38
1043+1105	16.9	16.8	3.1	2.3	121.3	0.9

Table 5 continued

Table 5 (continued)

Object	HST <i>I</i> -band			Gemini <i>K_s</i> -band			HST											
	AGN (mag) (2)	Spheroid (mag) (3)	Disk (mag) (4)	Bar (mag) (5)	AGN (mag) (6)	Spheroid (mag) (7)	Disk (mag) (8)	Bar (mag) (9)	n_{sph} (10)	R_{sph} ($''$) (11)	PA_{sph} (deg) (12)	q_{sph} (13)	R_{disk} ($''$) (14)	PA_{disk} (deg) (15)	q_{disk} (16)	R_{bar} ($''$) (17)	PA_{bar} (deg) (18)	q_{bar} (19)
1058+5259	18.3	16.9	16.7	17.3	1.9	0.63	22.6	0.86	5.94	32.4	0.73	2.58	44.3	0.33
1101+1102	19.1	15.4	15.7	5.0	3.0	173.8	0.77	4.59	144.1	0.48
1104+4334	20.6	15.8	18.7	18.6	4.5	2.79	21.2	0.81	2.79	70.3	0.49	1.46	32.9	0.31
1137+4826	22.9	17.5	17.5	2.6	0.24	83.0	0.76	1.29	103.5	0.7
1143+5941	18.7	17.5	16.5	17.5	2.4	0.5	118.8	0.9	6.72	7.0	0.65	4.26	5.9	0.3
1144+3653	16.3	15.8	15.0	1.4	1.2	29.2	0.79	7.87	11.5	0.79
1145+5547	19.3	18.2	15.3	18.0	1.0	0.52	54.3	0.68	7.0	67.8	0.66	2.1	58.1	0.33
1147+0902	16.6	15.9	18.2	3.8	2.01	105.6	0.72	2.01	138.2	0.36
1205+4959	17.2	16.6	15.7	2.0	0.68	169.9	0.88	4.41	162.1	0.88
1206+4244	17.4	17.2	15.5	17.1	1.0	0.64	138.0	0.98	7.0	104.9	0.98	2.57	134.7	0.33
1216+5049	18.4	15.0	14.9	3.3	2.75	79.2	0.5	8.03	72.9	0.33
1223+0240	16.6	15.3	15.0	5.0	3.51	167.4	0.83	4.3	174.2	0.77
1246+5134	19.1	17.9	17.1	2.0	0.4	87.0	0.52	2.88	91.7	0.25
1306+4552	20.9	18.3	15.6	17.1	1.0	0.3	171.6	0.91	5.05	127.4	0.91	2.88	152.9	0.36
1307+0952	19.1	17.4	15.3	19.4	1.0	0.56	136.1	0.85	4.59	174.0	0.66	0.27	86.6	0.4
1312+2628	17.5	17.9	15.5	17.9	1.0	0.45	173.8	0.88	6.03	169.5	0.88	2.7	0.0	0.22
1405-0259	18.8	17.4	15.6	1.0	0.77	59.3	0.59	5.01	64.6	0.4
1416+0137	18.5	15.9	15.2	2.4	1.57	158.7	0.85	6.75	132.4	0.67
1419+0754	17.6	16.1	14.5	1.9	0.98	21.8	0.72	6.45	18.5	0.68
1434+4839	17.7	16.3	15.0	16.4	1.5	0.88	153.2	0.89	6.29	156.4	0.83	3.98	150.5	0.32
1545+1709	18.7	16.2	16.9	5.0	1.49	62.0	0.59	2.42	60.1	0.2
1557+0830	17.9	16.8	2.5	1.16	58.7	0.78
1605+3305	17.9	16.9	16.5	1.2	0.68	97.0	0.66	3.82	82.8	0.61
1606+3324	18.6	16.3	16.5	3.3	1.16	18.0	0.7	4.29	20.2	0.48
1611+5211	18.8	15.8	16.2	3.1	0.75	126.6	0.81	4.62	106.3	0.68
1636+4202	18.4	15.8	17.1	18.2	5.0	3.0	22.4	0.73	3.0	9.1	0.45	0.33	100.2	0.45
1708+2153	16.6	16.5	16.3	1.9	1.54	73.5	0.69	6.95	70.6	0.49
2116+1102	18.1	17.6	16.0	19.0	1.2	0.5	50.4	0.87	5.95	80.7	0.87	1.96	86.6	0.34
2140+0025	16.5	17.3	16.8	...	15.0	17.0	15.7	...	1.0	0.47	79.3	0.71	2.24	88.3	0.71
2215-0036	17.0	18.1	16.7	1.0	0.5	82.7	0.46	3.45	83.1	0.4
2221-0906	17.6	17.6	17.3	...	16.6	17.6	15.9	...	2.7	0.86	24.5	0.69	2.98	81.6	0.69
2222-0819	17.4	18.7	15.6	17.8	15.0	25.9	14.7	16.6	1.1	0.33	77.7	0.93	3.98	78.3	0.93	1.48	108.2	0.32

Table 5 continued

Table 5 (continued)

Object	HST <i>I</i> -band			Gemini <i>K_s</i> -band			HST											
	AGN (mag) (2)	Spheroid (mag) (3)	Disk (mag) (4)	Bar (mag) (5)	AGN (mag) (6)	Spheroid (mag) (7)	Disk (mag) (8)	Bar (mag) (9)	n_{sph} (10)	R_{sph} ($''$) (11)	PA_{sph} (deg) (12)	q_{sph} (13)	R_{disk} ($''$) (14)	PA_{disk} (deg) (15)	q_{disk} (16)	R_{bar} ($''$) (17)	PA_{bar} (deg) (18)	q_{bar} (19)
2233+1312	17.9	17.9	15.9	17.5	16.2	16.4	14.8	16.2	1.0	0.38	65.9	0.66	7.71	57.1	0.53	1.82	25.6	0.51
2254+0046	17.0	17.4	17.6	1.1	0.26	113.0	0.91	1.91	79.6	0.9
2327+1524	17.9	14.7	14.8	...	15.1	13.5	14.1	...	2.4	1.71	3.9	0.75	7.86	6.8	0.75
2351+1552	17.7	17.0	16.9	...	16.5	16.1	15.8	...	2.0	0.77	92.5	0.63	2.69	104.4	0.49

NOTE—Surface-photometry fitting results using lenstronomy on HST and Gemini images. Col. (1): Target ID used throughout the text (based on R.A. and declination). Col. (2): Point-source (AGN) magnitude in HST *I*-band (uncertainty 0.1 mag). Col. (3): Spheroid magnitude in HST *I*-band (uncertainty 0.1 mag). Col. (4): Disk magnitude in HST *I*-band (if present; uncertainty 0.1 mag). Col. (5): Bar magnitude in HST *I*-band (if present; uncertainty 0.1 mag). Col. (6): Point-source (AGN) magnitude in Gemini *K_s*-band (uncertainty 0.2 mag). Col. (7): Spheroid magnitude in Gemini *K_s*-band (uncertainty 0.2 mag). Col. (8): Disk magnitude in Gemini *K_s*-band (if present; uncertainty 0.2 mag). Col. (9): Bar magnitude in Gemini *K_s*-band (if present; uncertainty 0.2 mag). Col. (10): Spheroid radius in arcseconds (10% uncertainty). Col. (11): Spheroid position angle (East of North) in degree (5 deg uncertainty). Col. (12): Disk radius in arcseconds (10% uncertainty). Col. (13): Spheroid axis ratio q ($=b/a$) (0.05 uncertainty). Col. (14): Disk radius in arcseconds (10% uncertainty). Col. (15): Bar radius in arcseconds (10% uncertainty). Col. (16): Disk axis ratio in degree (5 deg uncertainty). Col. (17): Bar axis ratio q ($=b/a$) (0.05 uncertainty). Col. (18): Bar position angle (East of North) in degree (5 deg uncertainty). Col. (19): Bar axis ratio q ($=b/a$) (0.05 uncertainty).

REFERENCES

- Abazajian, K. N., Adelman-McCarthy, J. K., Agueros, M. A., et al. 2009, *ApJS*, 182, 543
- Adelman-McCarthy, J. K., Agueros, M. A., Allam, Sahar S., et al. 2008, *ApJS*, 175, 297
- Astropy Collaboration, Robitaille, T. P., Tollerud, E. J. et al. 2013, *ã*, 558, A33
- Auger, M. W., Treu, T., Bolton, A. S., et al. 2009, *ApJ*, 705, 1099
- Batiste, M., Bentz, M. C., Raimundo, S. I., Vestergaard, M., & Onken, C. A. 2017, *ApJL*, 838, 10
- Beifiori, A., Courteau, S., Corsini, E. M., & Zhu, Y. 2012, *MNRAS*, 419, 2497
- Bennert, V. N., Treu, T., Woo, J.-H., et al. 2010, *ApJ*, 708, 1507
- Bennert, V. N., Auger, M. W., Treu, T., Woo, J.-H., & Malkan, M. A. 2011a, *ApJ*, 726, 59
- Bennert, V. N., Auger, M. W., Treu, T., Woo, J.-H., & Malkan, M. A. 2011b, *ApJ*, 742, 107
- Bennert, V. N., Treu, T., Auger, M. W., et al. 2015, *ApJ*, 809, 20
- Birrer, S., Amara, A., & Refregier, A. 2015, *ApJ*, 813, 102
- Birrer, S. & Amara, A. 2018, *Physics of the Dark Universe*, 22, 189
- Bradley, L., Sipocz, B., Robitaille, T., et al. 2016, *astropy/photutils: v.0.3*, doi:10.5281/zenodo.164986
- Brewer, B. J., Treu, T., Pancoast, A., et al. 2011, *ApJL*, 733, L33
- Bruzual, G., & Charlot, S. 2003, *MNRAS*, 344, 1000
- Cisternas, M., Jahnke, K., Bongiorno, A. et al. 2011a, *ApJ*, 741, 11
- Cisternas, M., Jahnke, K., Inskip, K. et al. 2011a, *ApJ*, 726, 57
- Courteau, S., de Jong, R. S., & Broeills, A. H. 1996, *ApJL*, 457, 73
- Courteau, S., Cappellari, M., de Jong, R. S., et al. 2014, *Reviews of Modern Physics*, 86, 47
- Croton, D. J. 2006, *MNRAS*, 369, 1808
- Davis, B. L., Graham, A. W., & Cameron, E. 2018, *ApJ*, 869, 113
- Davis, B. L., Graham, A. W., & Cameron, E. 2019, *ApJ*, 873, 85
- Decarli, R., Falomo, R., Treves, A., et al. 2010, *MNRAS*, 402, 2453
- DeGraf, C., Di Matteo, T., Treu, T., et al. 2015, *MNRAS*, 454, 913
- de Nicola, S., Marconi, A., & Longo, G. 2019, *MNRAS*, 490, 600
- Ding, X., Sliverman, J., Treu, T., et al. 2020, *ApJ*, 888, 37
- Di Matteo, T., Springel, V. & Hernquist, L. 2005, *Nature*, 433, 604
- Dubois, Y., Gavazzi, R., Peirani, S. & Silk, J. 2013, *MNRAS*, 433, 3297
- Dubois, Y., Peirani, S., Pichon, C., et al. 2016, *MNRAS*, 463, 3948
- Ferrarese, L., & Ford, H. 2005, *Space Science Reviews*, 116, 523
- Foreman-Mackey, D., Conley, A., Meierjürgen Farr, W. et al. 2013, *Astrophysics Source Code Library*, record ascl:1303.002
- Graham, A. W. 2008, *ApJ*, 680, 143
- Graham, A. W. 2016, *Astrophysics and Space Science Library*, 418, 263
- Graham, A. W., & Scott, N. 2013, *ApJ*, 764, 151
- Graham, A. W., Li, & I. -hui 2009, *ApJ*, 698 812
- Greene, J. E., & Ho, L. C. 2006, *ApJL*, 641, 21
- Greene, J. E., Peng, C. Y., Kim, M., et al. 2010, *ApJ*, 721, 26
- Greene, J. E., Strader, J., & Ho, L. 2020, *ARA&A*, 58, 257
- Gültekin, K., Richstone, D. O., Gebhardt, K., et al. 2009, *ApJ*, 698, 198
- Harris, W. E. 2018, *AJ*, 156, 296
- Harris, C. E., Bennert, V. N., Auger, M. W., et al. 2012, *ApJS*, 201, 29
- Hirschmann, M., Khochfar, S., Burkert, A., et al. 2010, *MNRAS*, 407, 1016
- Hopkins, P. F., Hernquist, L., Cox, T. J., Robertson, B., & Krause, E. 2007, *ApJ*, 669, 45
- Hopkins, P. F., Torrey, P., Faucher-Giguère, C.-A., Quataert, E., & Murray, N. 2016, *MNRAS*, 458, 816
- Hu, J., 2008, *MNRAS*, 386, 2242
- Hunter, J. D., *Computing in Science and Engineering*, 9, 90
- Into, T., & Portinari, L. 2013, *MNRAS*, 430, 2715
- Jahnke, K. & Maccio, A. 2011, *ApJ*, 734, 92
- Jahnke, K., Bongiorno, A., Brusa, M., et al. 2009, *ApJL*, 706, 215
- Kennedy, J. & Eberhart, R. C. 2001, *Academic Press*
- Kinney, A. L., Calzetti, D., Bohlin, R. C., et al. 1996, *ApJ*, 467, 38
- Kormendy, J. & Ho, L. C. 2013, *ARA&A* 51, 511
- Kormendy, J. & Kennicutt 2004, *ARA&A*, 42, 604
- Kormendy, J., Bender, R., & Cornell, M. E. 2011, *Nature*, 469, 374
- Läsker, R., Greene, J. E., Seth, A., et al. 2016, *ApJ*, 825, 1
- Li, Y.-R., Wang, J.-M., Ho, L. C., Du, P., & Bai, J.-M. 2013, *ApJ*, 779, 110
- , Lim, P. L., Diaz, R. I., & Laidler, V. 2015, *PySynphot User's Guide* (Baltimore, MD: STScI)

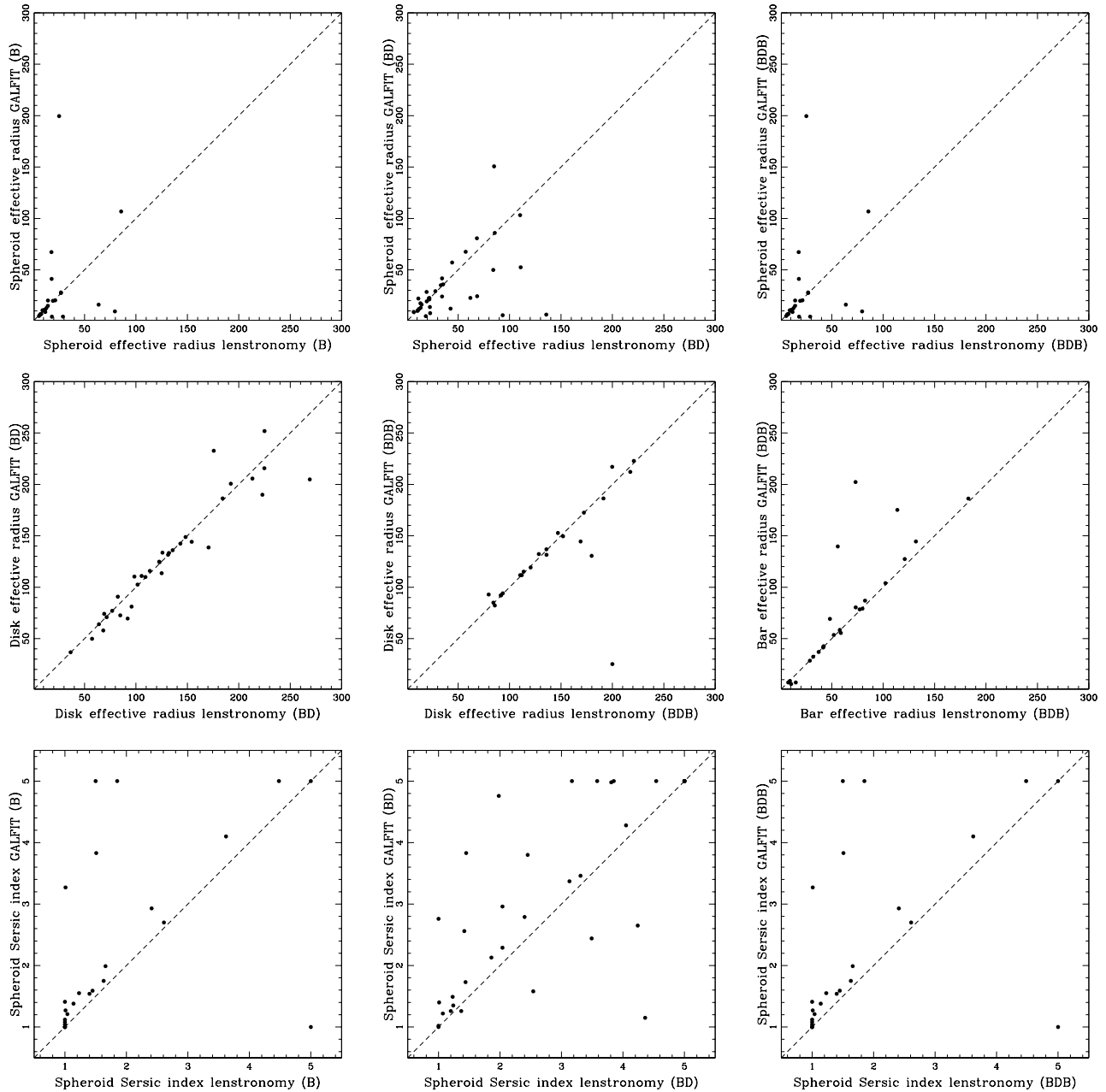


Figure 7. Comparison of fitting results using lenstronomy (x-axis) and GALFIT (y-axis) for effective radii (in pixels) and Sérsic index n for the different components (spheroid, disk, bar) in the different fits. To help guide the eye, the dashed-line represents the 1:1 correlation.

Marsden, C., Shankar, F., Ginolfi, M. & Zubovas, K. 2021, *Frontiers in Physics*, 8, 61
 Martin, G., Kaviraj, S., Volonteri, M. et al. 2018, *MNRAS*, 476, 2801
 McConnell, N. J. & Ma, C.-P., 2013, *ApJ*, 764, 184
 McConnell, N. J., Ma, C.-P., Gebhardt, K. et al. 2011, *Nature*, 480, 215
 McGill, K. L., Woo, J.-H., Treu, T., & Malkan, M. A. 2008, *ApJ*, 673, 703

Menci, N., Fiore, F., Bongiorno, A., & Lamastra, A. 2016, *A&A*, 594, 99
 Merloni, A., Bongiorno, A., Bolzonella, M., et al. 2010, *ApJ*, 708, 137
 Mortlock, D., Warren, S. J., Venemans, B.P., et al. 2011, *Nature*, 474, 616
 Onken, C. A., Ferrarese, L., Merritt, D., et al. 2004, *ApJ*, 615, 645
 Pancoast, A., Brewer, B. J., & Treu, T. 2011, *ApJ*, 730, 139

- Pancoast, A., Barth, A.J., Horne, K., et al. 2018, *ApJ*, 856, 108
- Park, D., Woo, J. H., Treu, T., et al. 2012 *ApJ*, 747, 30
- Park, D., Woo, J.-H., Bennert, V. N., et al. 2015, *ApJ*, 799, 164
- Peng, C. Y. 2007, *ApJ*, 671, 1098
- Peng, C., Ho, L. C., Impey, C. D. & Rix, H.-W. 2002, *AJ*, 124, 266
- Peng, C. Y., Impey, C. D., Ho, L. C., Barton, E. J., & Rix, H.-W. 2006a, *ApJ*, 640, 114
- Peng, C. Y., Impey, C. D., Rix, H.-W., et al. 2006b, *ApJ*, 649, 616
- Prsa, A., Harmanec, P. Torres, G., et al. 2016, *AJ*, 152, 41
- Rakshit, S., Stalin, C. S., & Kotilainen, J. 2020, *ApJS*, 249, 17
- Riechers, D. A., Walter, F., Carilli, C. L., & Lewis, G. F. 2009, *ApJ*, 690, 463
- Runco, J., Cosens, M., Bennert, V. N., et al. 2016, *ApJ*, 821, 33
- Saglia, R. P., Opitsch, M., Erwin, P., et al. 2016, *ApJ*, 818, 47
- Salviander, S., Shields, G. A., Gebhardt, K. & Bonning E. W. 2007, *ApJ*, 662, 131
- Sahu, N., Graham, A. W., & Davis, B. L., *ApJ*, 887, 10
- Sani, E., Marconi, A., Hunt, L.K., & Risaliti, G. 2011, *MNRAS*, 413, 1479
- Schlafly, E. F. & Finkbeiner, D. P. 2011, *ApJ* 737, 103
- Sérsic J. L., 1963, *Boletín de la Asociación Argentina de Astronomía La Plata Argentina*, 6, 41
- Sexton, R. O., Canalizo, G., Hiner, K.D., et al. 2019, *ApJ*, 878, 101
- Shankar, F., Bernardi, M., Sheth, R.K., et al. 2016, *MNRAS*, 460, 3119
- Shankar, F., Bernardi, M., Richardson, K., et al. 2019, *MNRAS*, 485, 1278
- Shen, Y. 2013, *BASI*, 41, 61
- Silverman, J. D., Treu, T., Ding, X., et al. 2019, *ApJL*, 887, 5
- Simmons, B., D., Smethurst, R. J., & Lintott, C. 2017, *MNRAS*, 470, 1559
- Tody, D. 1986, *SPIE*, 627, 733
- Tody, D. 1993, *ASPC*, 52, 173
- Tremaine, S., Gebhardt, K., Bender, R., et al. 2002, *ApJ*, 574, 740
- Treu, T., Malkan, M. A., & Blanford, R. D. 2004, *ApJL*, 615, 97
- van den Bosch, R. C. 2016, *ApJ*, 831, 134
- van Dokkum, P. 2001, *PASP*, 113, 1420
- Van Rossum, G., & Drake, F. L. 2009, *Python 3 Reference Manual*, Scotts Valley, CA: CreateSpace
- Vestergaard, M. 2002, *ApJ*, 571, 733
- Vestergaard, M. & Peterson, B. M. 2006, *ApJ*, 641, 689
- Virtanen, P., Gommers, R., Oliphant, T. E. et al. 2020, *Nature Methods*, 17(3), 261
- Wandel, A., Peterson, B. M., & Malkan, M. A. 1999, *ApJ*, 526, 579
- Weinzirl, T., Jogee, S., Kochfar, S., et al. 2009, *ApJ*, 696, 411
- Williams, P. R., Pancoast, A., Treu, T., et al. 2018, *ApJ*, 866, 75
- Williams, P. R., Pancoast, A., Treu, T., et al. 2020, *ApJ*, 902, 74
- Willmer, C. N. A. 2018, *ApJS*, 236, 47
- Woo, J.-H., & Urry, C. M. 2002, *ApJ*, 579, 530
- Woo, J.-H., Treu, T., Malkan, M. A., & Blandford, R. D. 2006, *ApJ*, 645, 900
- Woo, J.-H., Treu, T., Barth, A. J., et al. 2010, *ApJ*, 716, 269
- Woo, J.-H., Yoon, Y., Park, S., Park, D., & Kim, S. C. 2015, *ApJ*, 801, 1
- Yang, L., Roberts-Borsani, G., Treu, T., Birrer, S., Morishita, T., & Bradac, M. 2021, *MNRAS*, 501, 1028